IOPscience iopscience.iop.org

Home Search Collections Journals About Contact us My IOPscience

Magnetic structures of Laves phase superlattices

This article has been downloaded from IOPscience. Please scroll down to see the full text article.

2003 J. Phys.: Condens. Matter 15 4301

(http://iopscience.iop.org/0953-8984/15/25/303)

View the table of contents for this issue, or go to the journal homepage for more

Download details:
IP Address: 171.66.16.121
The article was downloaded on 19/05/2010 at 12:23

Please note that terms and conditions apply.

INSTITUTE OF PHYSICS PUBLISHING JOURNAL OF PHYSICS: CONDENSED MATTER

J. Phys.: Condens. Matter **15** (2003) 4301–4330 PII: S0953-8984(03)61195-1

Magnetic structures of Laves phase superlattices

M J Bentall[1,3], R A Cowley[1], W J L Buyers[2], Z Tun[2], W Lohstroh[1,4], R C C Ward[1] and M R Wells[1]

[1] Oxford Physics, Clarendon Laboratory, Parks Road, Oxford OX1 3PU, UK
[2] Neutron Program for Materials Research, National Research Council of Canada, Chalk River, ON, KOJ 1JO, Canada

E-mail: m.bentall1@physics.ox.ac.uk and r.cowley1@physics.ox.ac.uk

Received 21 March 2003
Published 13 June 2003
Online at stacks.iop.org/JPhysCM/15/4301

Abstract

We present a determination of the magnetic structures of three Laves phase superlattice samples of structure $[70/30]_{60}$, $[150/100]_{50}$, and $[50/70]_{60}$, where the structure is given as $[t_1$ Å $DyFe_2/t_2$ Å $YFe_2]_N$, grown by molecular beam epitaxy. The experiments were performed using magnetization measurements and neutron scattering measurements at the NRU reactor at Chalk River in Canada.

For the $[70/30]_{60}$ sample, a magnetic field parallel to the scattering vector, $\boldsymbol{Q}$, was applied to determine the nuclear component of the scattered intensity. The magnetic structure with the field aligned along the [001] had all the moments aligned along the field direction and the magnitude of the moment on the iron site was temperature independent with a value of 2.3(0.3) μ_B. The moment on the dysprosium site was found to decrease with temperature from about 10 μ_B to a value of 6(0.5) μ_B at 300 K. When the field was applied in the $[1\bar{1}0]$ direction the magnetic moments were found to rotate out of the (110) epitaxial plane towards the [110] direction by an angle $\psi = 10°$ at 300 K, which increased at 4 K to an angle of $\psi = 40°$ close to the [100] out-of-plane direction.

For the $[150/100]_{50}$ sample, when a 6 T magnetic field was applied along the $[1\bar{1}0]$ direction, the main peak of the magnetically sensitive $(11\bar{1})$ reflection was found to decrease in intensity while the scattering at the satellite peaks increased. This change in intensity is due to the formation of magnetic exchange springs in the 'soft' YFe_2 layers of the superlattice. Detailed measurements around the $(11\bar{1})$ reflection and calculations for an exchange spring model give excellent agreement between the model and the experiment.

Finally, the $[50/70]_{60}$ sample showed unexpected behaviour because the moments aligned largely perpendicular to an applied field. This is similar to a

[3] Author to whom any correspondence should be addressed.
[4] Present address: Division of Physics and Astronomy, Faculty of Sciences, Vrije Universiteit De Boelelaan, 1081 HV Amsterdam, The Netherlands.

spin-flop phase of an antiferromagnet and it is argued that this occurs because the net moments on the $DyFe_2$ and YFe_2 layers are nearly equal.

(Some figures in this article are in colour only in the electronic version)

1. Introduction

There is considerable interest in the magnetic properties of Laves phase superlattices. The interest is twofold—firstly, these structures present, theoretically at least, the possibility of developing hard magnets whose performance parameter, the magnetic energy product $(BH)_{MAX}$, is as large as 1 MJ m^{-3}, provided that the exchange spring mechanism can be suppressed [1]. These would have many potential technical applications as sensors and magnetic read heads exploiting their giant-magnetoresistance properties; a change in resistance, $\Delta R/R$, of 32% has been demonstrated in an applied field of 23 T [2].

Secondly, research into the Laves phase superlattices is a natural extension of the 1970s research on the bulk Laves phases [3], and of the more recent research into rare-earth superlattices [4–7].

The superlattices we have studied are composite systems of hard and soft magnetic materials, in which the magnetization of the hard material may be tied to an easy direction, whereas the magnetization of the soft magnetic material may be altered by the application of an external magnetic field.

Recent studies have shown the existence of the so-called spring magnet behaviour [8, 9]. This arises when the net magnetization of the hard $DyFe_2$ layer is larger than that of the YFe_2 layer, with the result that the easy direction of magnetization is determined largely by these hard layers. The iron moments in the soft YFe_2 layers couple parallel to those in the $DyFe_2$ layers through the strong exchange interaction. If a magnetic field is applied above a critical bending field, the iron moments in the YFe_2 layers tend to rotate parallel to the field direction to reduce their Zeeman energy and there is a field range where the magnetic behaviour is perfectly reversible.

Another interesting magnetic structure arises when the magnetization of the YFe_2 layers dominates the magnetic behaviour. In this case, when a magnetic field is applied it can be favourable for the iron moments in the YFe_2 layers to all align parallel to the field while the net moment in the $DyFe_2$ layers is antiparallel to the applied field direction. This behaviour has been shown to cause negative coercivity in some samples [10–14].

The explanation of these effects relies heavily on the superlattices having a high degree of modulation (so the effects of interdiffusion and roughness between the bilayers of the superlattice are minimal) of the hard and soft magnetic layers. We have previously [15] carried out a structural study of seven Laves phase superlattice samples using x-ray diffraction and high-resolution electron microscopy (HREM) techniques. This has shown that the Laves phase superlattices grown using the Balzers facility, Oxford, are of high quality and exhibit a high degree of modulation. The results [15] show that a typical sample has a mosaic spread of 0.9° and a superlattice coherence length, ξ, of 2000 Å.

Mössbauer studies [16] on bulk $DyFe_2$ suggest that the easy direction of magnetization lies along $\langle 001 \rangle$ for all temperatures, and is controlled mainly by the crystal field interaction at the rare-earth site. However, studies [17, 18] of epitaxial $DyFe_2$ thin layers grown on (110) planes have shown that the easy direction of magnetization is not always in the same direction as that of bulk $DyFe_2$. The elastic strains produced by epitaxial growth of Laves phase thin films mean

that the easy direction is temperature dependent, and is a result of the competition between the magnetoelastic and anisotropy energies. The [001] direction is the easy direction at a temperature of 4 K, and there is a steady rotation towards [$\bar{3}$51] as the temperature approaches 300 K [19]. Because the $DyFe_2$ layer is magnetically 'hard' and the YFe_2 layer is magnetically 'soft', it is expected that in $DyFe_2$-dominated superlattices, the easy direction will be mainly controlled by the magnetic properties of the $DyFe_2$ layer. However, metastable states in $DyFe_2$ layers have been observed at 100 K [20] with applied fields of 23 T. It is generally agreed that there are three magnetic interactions that couple the moments of the rare-earth and transition metal sites in the Laves phases. For $DyFe_2$ these are

(1) the transition metal–transition metal interaction ($J_{T-T} \sim 600$ K),
(2) the rare-earth–transition metal interaction ($J_{R-T} \sim 100$ K), and
(3) the rare-earth–rare-earth interaction ($J_{R-R} \sim 30$ K), where J is the exchange coupling constant.

The coupling between rare-earth moments is by far the weakest interaction, due to the small overlap of the 4f wavefunctions. This interaction may couple the rare-earth moments parallel or antiparallel to one another. In $DyFe_2$ and YFe_2, the exchange coupling between the iron moments is large, so at the $DyFe_2$–YFe_2 interface of the superlattice, the iron moments on either side of the interface tend to align parallel to one another via the strong exchange interaction.

The coupling between the rare-earth and the transition metal moments in the hard $DyFe_2$ layers occurs from the effective coupling of the 3d electrons in the transition metal with the 4f electrons of the rare-earth metal. This interaction occurs via 5d–4f coupling through hybridized 5d–3d states. This results in an antiparallel alignment between the rare-earth and transition metal moments for the heavy rare earths [21].

When a magnetic field is applied to a Laves phase superlattice there can be a variety of different magnetic structures, some of which are shown in figure 1. If the field is sufficiently large, all the moments are aligned parallel to the applied field, as shown in figure 1(d). The field is then larger than B_C, the field needed to overcome J_{R-T}. At very low fields the iron moments in both the $DyFe_2$ and YFe_2 are antiparallel to the rare-earth moments. We shall denote this as a ferrimagnetic state, figure 1(a). At intermediate fields beyond a critical 'bending field', B_B, an exchange spring structure may be favoured, figure 1(b), in which the $DyFe_2$ net moment is aligned along the field while the iron moments in the YFe_2 layers vary in direction to minimize the net energy at the interface and the Zeeman energy that results from the interaction of the iron moments with the applied magnetic field. We shall show in section 4 that there are also phases in which the moments align almost perpendicular to the applied field and we denote these as spin-flop structures. Clearly when the effects of anisotropy, metastability, and different thicknesses of $DyFe_2$ and YFe_2 are also considered, there can be a wide variety of magnetic behaviour for these superlattices as we shall discuss later.

We are unaware of any previous neutron scattering studies of the magnetic structures of Laves phase superlattices. The experiments are technically difficult because the magnetic structures are ferromagnets and so the magnetic scattering must be separated from the nuclear scattering. Furthermore the ferromagnetic transition temperature is around 600 K at which temperature diffusion rapidly destroys the superlattices so the nuclear scattering cannot be measured at a temperature above T_c. Because of these difficulties we initially attempted to use polarized neutrons with the E1 spectrometer at HMI, Berlin. The experiment was unsuccessful because:

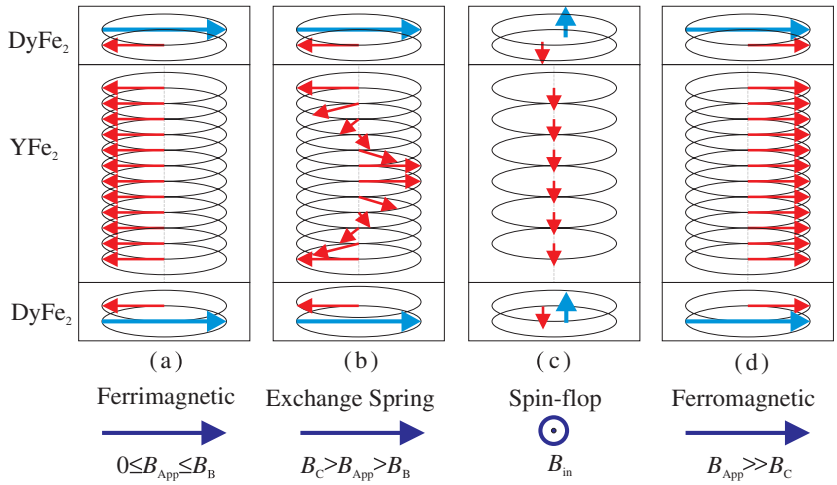

Figure 1. A schematic view of an exchange spring, ferrimagnetic, spin-flop, and ferromagnetic state in a $DyFe_2$–YFe_2 multilayer. The long arrows represent the dysprosium moment while the short arrows represent the iron moment. The arrows below each panel show the direction of the applied field, and for the spin-flop structure, the length and number of arrows representing the moments has been reduced for clarity.

(i) The Laves phase superlattice depolarized the scattered beam even when in an applied field of 4 T.

(ii) The flux of polarized neutrons was low so the counting times were very long and it was difficult to align the superlattice.

We have therefore used unpolarized neutron scattering techniques at Chalk River and have performed two types of experiment. The results obtained with both of these configurations are detailed in section 4. The results are discussed in a final section.

2. Experimental arrangements

2.1. Sample growth

Bulk $DyFe_2$ and YFe_2 crystallize in a face-centred cubic diamond structure with eight RFe_2 units per cubic unit cell. This structure consists of an array of corner-shared tetrahedra of iron atoms, surrounded by two rare-earth atoms. The structure is schematically illustrated in figure 2. The samples were grown using the molecular beam epitaxy (MBE) facility in the Clarendon Laboratory, Oxford. Sapphire substrates with a $(11\bar{2}0)$ orientation were cleaned and 1000 Å of (110) niobium was deposited as a chemical buffer layer, followed by a 20 Å iron 'seed' to improve crystal growth [22]. The superlattice was then grown by co-deposition of the elementary fluxes and the [110] direction was the growth axis. The growth process was monitored *in situ* using RHEED diffraction. The best samples were obtained with an initial growth temperature of 600 °C for the superlattice, which was subsequently reduced to 450 °C over the course of the first few superlattice repeats. The epitaxial relationships are $(11\bar{2}0)$ sapphire ∥ (110) Laves, (0001) sapphire ∥ $(1\bar{1}1)$ Laves, and $(\bar{1}100)$ sapphire ∥ $(\bar{1}12)$ Laves. The structure of the samples is shown in figure 3.

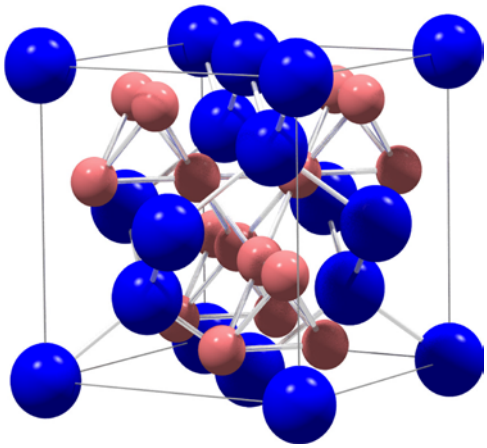

Figure 2. The conventional unit cell of the C15 Laves phases $DyFe_2$ and YFe_2. The large spheres represent dysprosium or yttrium atoms and the small spheres represent iron atoms. They crystallize in the face-centred cubic structure O_h^7 ($Fd\bar{3}m$) with 24 atoms per cubic unit cell.

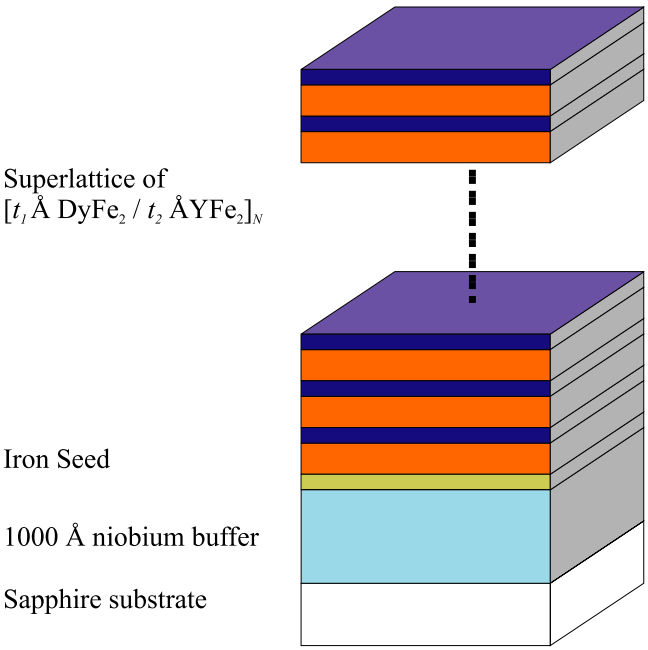

Figure 3. A schematic view of a Laves phase superlattice sample grown by MBE.

2.2. *Structure of the superlattices*

All of the superlattices were initially investigated using x-ray diffraction to determine their structural quality. The detailed results, presented elsewhere [15], showed that the samples exhibited a high degree of modulation, with interface widths of typically ∼10 Å, mosaic spreads of ∼0.9°, and superlattice coherence lengths of ∼2000 Å. The results of fitting a model to three Bragg reflections using a Rietveld refinement with a differential evolutionary algorithm gave excellent agreement with the experimental data, and are summarized in table 1.

Table 1. The structural parameters of the $DyFe_2$–YFe_2 superlattices as determined from x-ray diffraction measurements at room temperature [15]. The nominal and measured structures are given as $[t_1$ Å $DyFe_2/t_2$ Å $YFe_2]_N$, where N is the number of bilayer repeats. ξ is the superlattice coherence length. λ_1 and λ_2 are the concentration and strain profile widths of the superlattices. d_1 and d_2 are the average lattice parameters of the $DyFe_2$ and YFe_2 blocks along the growth axis respectively, and Υ is the rocking curve FWHM. The errors are estimated piecewise at a 5% level of the error function.

Sample	SL989	SL1003	SL990
Nominal structure	$[70/30]_{60}$	$[150/100]_{50}$	$[50/70]_{60}$
Measured structure	$[73/24]_{60}$	$[152/88]_{50}$	$[55/67]_{60}$
ξ (Å)	1800(200)	2300(200)	1700(200)
λ_1 (Å)	9(1)	19(6)	14(2)
λ_2 (Å)	13(2)	19(2)	12(2)
d_1 (Å)	7.281(0.002)	7.280(0.001)	7.270(0.001)
d_2 (Å)	7.356(0.005)	7.349(0.001)	7.332(0.001)
Υ (deg)	0.987(0.001)	0.850(0.002)	0.874(0.002)

2.3. Neutron scattering experiments

The magnetic structure of the samples was determined with the DUALSPEC C5 triple-axis neutron spectrometer at the NRU reactor, Chalk River Laboratories, Canada. The horizontal collimations from reactor to detector were 0.4°–0.477°–0.85°–2.4°. Neutrons with an energy of 14.56 meV were selected by the (002) reflection of a pyrolytic graphite (PG) monochromator. Higher-wavelength harmonics were eliminated with a PG filter, and a PG analyser was placed in the scattered beam. The samples were mounted in a 3 T horizontal field or 6.5 T vertical field cryomagnet depending upon the configuration. The sample temperatures were in the range of 3.0–300 K.

The magnetic structures of samples SL989 and SL990, as a function of temperature and applied magnetic field, were determined in a horizontal field magnet cryostat with the sample mounted such that the [110] growth axis was vertical and the $[1\bar{1}0]$ and [001] directions were in the $(hh0)$ scattering plane. For this configuration, the superlattice growth plane was parallel to the scattering plane and the scattering vector, $\boldsymbol{Q}$, was perpendicular to the growth direction. In this configuration the superlattice peaks could not be observed but the field direction could be aligned in any chosen direction in the plane of the superlattice. Both radial and transverse wavevector scans were made through the centre of the Bragg peaks. This arrangement is unusual in that the sample is edge on to the incident and scattered beams, and this is schematically illustrated in figure 4(a). Another configuration was needed to probe the exchange spring structure of sample SL1003, and this is shown in figure 4(b). A vertical field was applied parallel to the $[1\bar{1}0]$ direction, while the wavevector transfer $\boldsymbol{Q}$ could be scanned through the main Bragg peaks as well as their associated superlattice peaks in the $(h\bar{h}0)$ plane. The scattering wavevector was varied parallel and perpendicular to the film surface, through the centre of the Bragg or satellite peak. The scans were defined by two components $\boldsymbol{Q} = (\boldsymbol{q}_x, 0, \boldsymbol{q}_z)$, where $\boldsymbol{q}_z \parallel [111]$ and $\boldsymbol{q}_x \parallel [001]$. Scans in which $\boldsymbol{q}_x$ were varied are referred to as transverse scans while those in which $\boldsymbol{q}_z$ varies are referred to as longitudinal scans. The Bragg reflections are given in the usual Miller index notation (hkl), where each of the indices is related to the $\boldsymbol{q}$-components and the units are $\frac{2\pi}{a}$. The in-plane experimental resolution was typically 0.015 Å^{-1}.

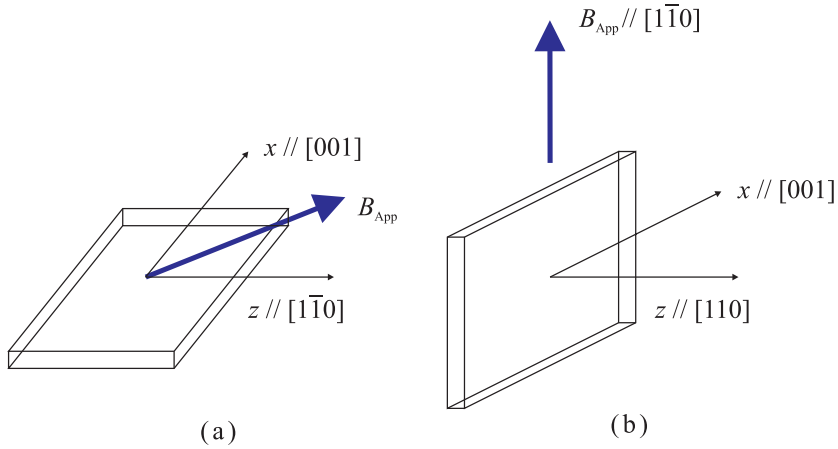

Figure 4. A schematic diagram showing the two configurations used in the neutron scattering experiments.

3. Neutron scattering

Neutrons are scattered by the nuclei and by the magnetic moments in a material. For the ferromagnetic Laves phases both components give rise to scattered intensity at the Bragg peaks.

3.1. Neutron–nuclear scattering

The coherent nuclear Bragg scattering component is given by

$$\left(\frac{\mathrm{d}\sigma}{\mathrm{d}\Omega}\right)_{\mathrm{coh}} = \left|\sum_i b_i \mathrm{e}^{\mathrm{i}\boldsymbol{Q}\cdot\boldsymbol{R}_i}\right|^2, \tag{1}$$

where b_i is the mean bound coherent scattering length, and we have neglected the Debye–Waller factor. The incoherent scattering length contributes to the background, as does random chemical disorder. The sum over i runs over the entire superlattice structure.

Equation (1) can be simplified if we neglect planar disorder effects, and assume that the bilayers are identical, so that the superlattice can be decomposed into a series of repeating bilayer structures. For experiments where $\boldsymbol{Q}$ was parallel to the $\boldsymbol{q}_z = [110]$ growth direction, the coherent nuclear cross-section is then proportional to

$$\left(\frac{\mathrm{d}\sigma}{\mathrm{d}\Omega}\right)_{\mathrm{coh}} \propto \left|\left(\sum_{S=0}^{N-1} \mathrm{e}^{\mathrm{i}q_z\bar{\Lambda}S}\right)\left(\sum_{j=0}^{n_1+n_2-1} b_j \mathrm{e}^{\mathrm{i}q_z r_{zj}}\right)\right|^2, \tag{2}$$

where N is the number of bilayer repeats, of average width $\bar{\Lambda}$, q_z is the wavevector transfer parallel to the growth direction and n_1 and n_2 are the number of planes of constituent 1 or 2 in the bilayer. j is summed over the planes within a bilayer and r_{zj} is the z-component of the position of each plane. This approximation has been discussed by several authors for the analogous case of x-ray charge scattering from various superlattice structures [7, 23, 24], and was used by us to determine the structures of the $DyFe_2$–YFe_2 Laves phase superlattices [15].

The first factor in equation (2) gives rise to a series of peaks corresponding to the scattering from planes with an average spacing $\bar{\Lambda}$, and it is convenient to index them as

$$q_z = \frac{2\pi l}{\bar{d}} + \frac{2\pi m}{\bar{\Lambda}} \tag{3}$$

where $m = 0, \pm 1, \pm 2, \ldots$ is the order of the satellite, l is the index of the Bragg reflection, and $\bar{d}$ is the average lattice spacing. The second factor is the one-bilayer structure factor, and is an envelope function that modifies the intensity of the peaks and is usually a maximum when $m = 0$.

We calculated the neutron nuclear scattering from the known x-ray structure and the mean bound scattering lengths, b_i, are given in the *International Tables for Crystallography* [25]. The structure obtained using x-ray techniques [15] was modelled using equation (1), with the sum running over the entire superlattice structure. This equation was also used to model the exchange spring structure described in section 3.3. The superlattice model then includes the effect of a varying strain profile, due to the different lattice constants of $DyFe_2$ and YFe_2, and a concentration profile arising from the effect of interdiffusion due to the elevated growth temperature and interfacial roughness. This is described with tanh functions in a similar way to in the method used for the x-ray scattering data. The precise form of the concentration and strain profiles is given in [15].

3.2. Neutron magnetic scattering

For unpolarized neutrons, the elastic magnetic cross-section can be written as

$$\left(\frac{\mathrm{d}\sigma}{\mathrm{d}\Omega}\right)_{\mathrm{mag}} = \left(\frac{\gamma r_0}{2}\right)^2 \sum_{i,j} f_i^{\star}(\boldsymbol{Q}) f_j(\boldsymbol{Q}) \sum_{\alpha,\beta} (\delta_{\alpha\beta} - \hat{Q}_\alpha \hat{Q}_\beta) \mathrm{e}^{\mathrm{i}\boldsymbol{Q}\cdot(\boldsymbol{R}_i - \boldsymbol{R}_j)} \langle J_{i\alpha}\rangle \langle J_{j\beta}\rangle g_{i\alpha} g_{j\beta}, \tag{4}$$

where $r_0 = (e^2/4\pi\epsilon_0 m_{\mathrm{e}} c^2) = 2.82 \times 10^{-15}$ m, which is the classical radius of the electron, γ is the neutron gyromagnetic ratio ($=-1.913$), g is the Landé factor, $f_j(\boldsymbol{Q})$ is the magnetic form factor, $g_{j\beta}\langle J_{j\beta}\rangle$ is the average of the β-component of the magnetic moment on site j, and α and β are Cartesian coordinates.

The term $(\delta_{\alpha\beta} - \hat{Q}_\alpha \hat{Q}_\beta)$, which arises from Fourier transforming the angle-dependent dipolar interaction, selects only the components of the magnetic moment that are perpendicular to the scattering vector $\boldsymbol{Q}$, and was calculated once $\boldsymbol{Q}$ and the angle of the magnetization were known.

We shall require the scattering cross-sections for each of the different magnetic structures illustrated in figure 1. The scattering from the ferromagnetic, spin-flop, and ferrimagnetic structures will not be given in detail as they are readily obtained using equation (4). The magnetic form factor, $f_j(\boldsymbol{Q})$, is obtained from [25].

3.3. The exchange spring structure

The neutron scattering from the exchange spring structure requires more discussion. At moderately high temperatures, the anisotropy of the dysprosium lattice can be overcome with the result that its moment follows the applied field. The simplest model is then to assume that the magnetization of the dysprosium moments follows the magnetic field. In the YFe_2 layers, the iron moments will at low fields be opposite to the field direction, but at larger fields they will rotate to gain Zeeman energy. A continuum approximation then gives the angle of rotation of the iron moments of constant length in the soft layer as

$$\sin\frac{1}{2}\theta_z = \sqrt{p}\, sn\left[2K(p)\left(\frac{z}{D}\right)\right], \tag{5}$$

where $D = \sqrt{2}n_2 d_2/8$ is the thickness of the spring in the $YFe_2(110)$ layer, and n_2 is the number of atomic planes for these layers, $\theta_z = 180°$ ($\|[1\bar{1}0]$) at $z = 0$ and D. Thus the outermost layers of the spring are antiparallel to the dysprosium moment and to the field. Within the spring the iron moment rotates in the epitaxial (110) plane. The Jacobi elliptic function is denoted as sn, and $K(p)$ is a complete elliptic integral of the first kind that can be shown to be given by

$$K(p) = \int_0^{\pi/2} \frac{\mathrm{d}\theta}{\sqrt{1 - p\sin^2\theta}}. \tag{6}$$

K can also be determined using the relation [26]

$$K = \pi\sqrt{\frac{B_{\mathrm{App}}}{B_{\mathrm{B}}}}, \tag{7}$$

where B_{App} is the applied magnetic field, and B_{B} is the critical bending field. The exchange spring solution is the lowest-energy state if $K(p)$ is greater than π or if the applied magnetic field, B_{App}, is greater or equal to the critical bending field B_{B}. The exchange spring structure shown in figure 1(b) is then one of a chiral pair of solutions to equation (5). Since we performed unpolarized neutron scattering, these two solutions were indistinguishable. If B_{App} is less than B_{B}, then the ferrimagnetic state shown in figure 1(a) is the stable state. For discrete symmetric exchange springs confined to the soft YFe_2 layers, the bending field is given by [26]

$$B_{\mathrm{B}} = J_{\mathrm{T-T}}\left(\frac{\pi}{n_2}\right)^2 \tag{8}$$

where $J_{\mathrm{T-T}}$ is ~600 K or ~800 T [9]. The angles of the moments can be calculated by first obtaining the bending field using equation (8). K is then calculated using equation (7) and p is obtained iteratively using equation (6). This allows $\langle J_{j\beta}\rangle$, the components of the moments, to be determined as a function of layer through equation (5). The result of this procedure is illustrated in figure 13 for SL1003 in an applied field and will be discussed in detail later.

4. Experimental results

4.1. The ferrimagnetic structures of SL989: $[70/30]_{60}$

4.1.1. Nuclear scattering and preliminaries. X-ray scattering measurements have determined the $DyFe_2$ and YFe_2 layer widths (table 1). The narrow YFe_2 layer thickness of this sample means that the bending field before the onset of the exchange spring state is of the order of 22 T, with $n_2 = 19$ and $J_{\mathrm{T-T}} \sim 800$ T. This field is much higher than the maximum field available with the cryomagnets used, and so the lowest-energy magnetic configuration is likely to be a ferrimagnetic structure, schematically illustrated in figure 1(a).

The sample was mounted so that the (110) growth plane was in the scattering plane in which the magnetic field was applied, figure 4(a), as described in section 2.3. The scattered intensity was measured for the $(2\bar{2}0)$, $(1\bar{1}\bar{1})$, $(2\bar{2}\bar{2})$, $(1\bar{1}\bar{3})$, and $(00\bar{4})$ Bragg reflections, for temperatures in the range 4–300 K. The magnetic field (=2.6 T) was applied mostly along either the $(1\bar{1}0)$ or the [001] directions. We believe that this field was sufficient to orient most of the magnetic domains into a single domain. Some measurements were made at room temperature by applying the magnetic field parallel to the wavevector transfer of each Bragg reflection in turn; if the magnetic moments follow the applied field, the magnetic scattering is then absent and the intensities give a measure of the nuclear Bragg reflections.

Table 2. The Laves phase scattering amplitudes and the nuclear scattering for SL989 $[70/30]_{60}$. The scattering amplitude is the nuclear structure factor, the normalization (column 3) is the factor by which the observed intensity is divided to give a quantity proportional to the square of the structure factor (column 4), the calculated scattering. The observed scattering is background subtracted, normalized, and corrected to a constant monitor and for resolution effects. The ratio of the observed to calculated scattering is R. The mean rare-earth (iron) scattering length is b_1 (b_2).

Reflection	Scattering amplitude	Normalization	Calculated scattering	Observed scattering	Ratio R
$(00\bar{4})$	$-2b_1 + 4b_2$	1	0.75	5(5)	7(7)
$(1\bar{1}3)$	$-\sqrt{2}b_1 - 2b_2$	1.716	15.61	100(5)	6.4(0.3)
$(1\bar{1}\bar{1})$	$\sqrt{2}b_1 - 2b_2$	4.24	0.03	2(5)	70(200)
$(2\bar{2}\bar{2})$	$4b_2$	1.525	14.29	102(5)	7.1(0.3)
$(2\bar{2}0)$	$-2b_1$	2.55	8.49	32(3)	3.7(0.3)

One advantage of the cubic Laves phases is that their structure factors are particularly simple, as listed in table 2. In particular, the $(2\bar{2}0)$ reflection depends solely on the rare-earth scattering while the $(2\bar{2}\bar{2})$ reflection depends solely on the iron scattering. The integrated intensities of the Bragg reflections were mostly measured by performing scans in which the wavevector transfer was varied either longitudinally or transversely to the Bragg reflections. The data were fitted using a conventional Levenberg–Marquardt algorithm to a single Gaussian lineshape and a sloping background. The fits gave the intensity, width, and position of the peaks. Since the measurements were performed with a triple-axis spectrometer, neither the peak intensity nor the integrated intensity are directly proportional to the square of the structure factors. The normalization factor [27] depends upon the scattering angles, the horizontal collimations, the mosaic spreads of the monochromator and analyser, and the scan direction in reciprocal space. The relative corrections have been calculated in the limit of negligible sample mosaic spread and in the limit where the sample mosaic spread dominates the transverse resolution, as is the case for most of these experiments. Rather unexpectedly, both limits gave the same relative corrections within the experimental errors, and the normalization factors shown in table 2 were calculated and are chosen to be unity for the $(00\bar{4})$ Bragg reflection. The observed nuclear scattering was obtained at 296 K when the 2.6 T magnetic field was applied parallel to the wavevector transfer, so that the magnetic scattering would not contribute to the scattering. The results in table 2 give the relative measured nuclear structure factor squared. They are compared with those calculated using the chemical structure deduced from x-ray measurements as detailed in table 1. The ratio, R, of the observed intensity to the calculation is also listed in table 2. The ratio is reasonably constant except for the $(1\bar{1}\bar{1})$ reflection for which the nuclear scattering is so small that R is not well determined from the data, and for the $(2\bar{2}0)$ reflection for which R is much smaller.

We have no explanation for the low intensity observed for the $(2\bar{2}0)$ reflection; possibly there may be an unexpected problem of alignment or of absorption associated with the unusual sample alignment with the plane of the sample being parallel to the scattering plane. We shall therefore put the magnetic scattering on an absolute scale by using the average ratio of $R = 6.8$, except for the $(2\bar{2}0)$ reflection for which we shall use the observed ratio of $R = 3.7$.

4.1.2. Magnetic structure with the magnetic field along [001]. The simplest model of the ferrimagnetic structures, shown in figure 1(a), assumes that all the iron moments are parallel, and lie antiparallel to the rare-earth moments. This is expected because the applied field is much less than the bending field of the relatively thin YFe_2 layer, and because of the strong exchange

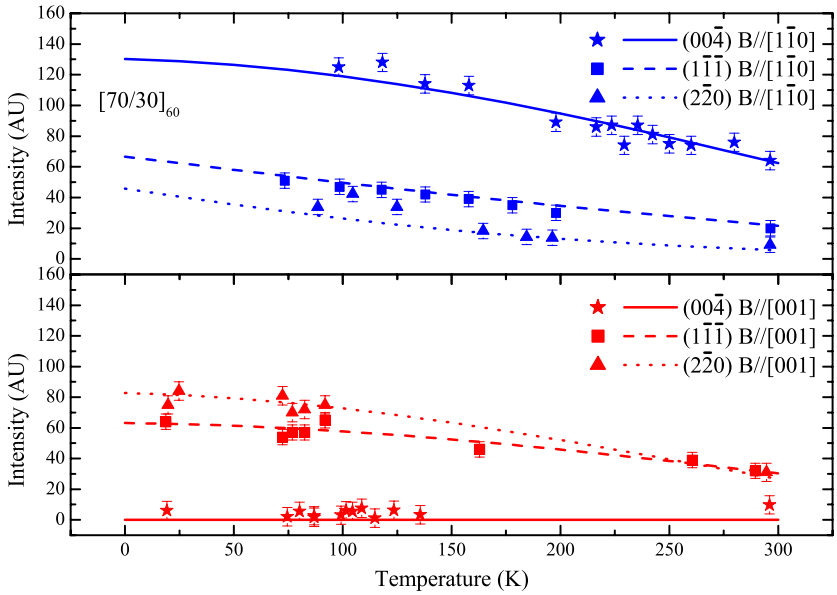

Figure 5. The resolution-corrected magnetic component of the intensities of the reflections as a function of temperature for two applied field directions. The curves are calculated using the model described in the text.

interaction between the transition metal ions. The dysprosium moments are antiparallel to the iron moments because the 4f–3d exchange coupling arising from 5d–3d hybridization is antiferromagnetic [21]. The applied magnetic field, in the presence of magnetic anisotropy, is expected to rotate this spin structure.

The magnetic structure factor for the different reflections can be obtained if the nuclear scattering lengths, b_1, in table 2 are replaced by $0.2702 c_{\mathrm{Dy}} f_{\mathrm{Dy}} \mu_{\mathrm{Dy}}$, where $c_{\mathrm{Dy}} = 0.7523$ is the fraction of Dy and Y planes that contain Dy, f_{Dy} is the dysprosium magnetic form factor, and μ_{Dy} is the ordered Dy magnetic moment in μ_{B}, and b_2 is replaced by a similar expression involving the iron form factor and moment. The numerical factor of 0.2702 converts the magnetic scattering amplitude to the same units as the nuclear scattering length, b. The magnetic contributions to the intensities of the Bragg reflections were obtained from the total scattered intensities by subtracting the nuclear components which were assumed to be temperature independent. The results are shown in figure 5 for the magnetic scattering when the field was applied in the [001] and [1$\bar{1}$0] directions as the sample was cooled from room temperature.

When the field was applied in the [001] direction, figure 4(a), there was very little if any magnetic scattering for the (00$\bar{4}$) Bragg reflection showing that the moments are aligned along the field direction as expected, and the (2$\bar{2}$0) intensity is largest since the moments are perpendicular to $\boldsymbol{Q}$. The temperature dependence of the magnetic moment on the Dy atoms was deduced from the (2$\bar{2}$0) Bragg reflection using the expressions for the structure factor to give

$$\mu_1 = \frac{1}{2 f_{\mathrm{Dy}} c_{\mathrm{Dy}}} \left(\frac{I_{\mathrm{M}}}{R(0.073)} \right)^{1/2} = 1.4450 \sqrt{I_{\mathrm{M}}} \tag{9}$$

where $f_{\mathrm{Dy}} = 0.885$, $c_{\mathrm{Dy}} = 0.7523$, and $R = 3.7$. I_{M} is the quantity for magnetic intensity analogous to the nuclear observed scattering (column 5) of table 2. The results are shown in

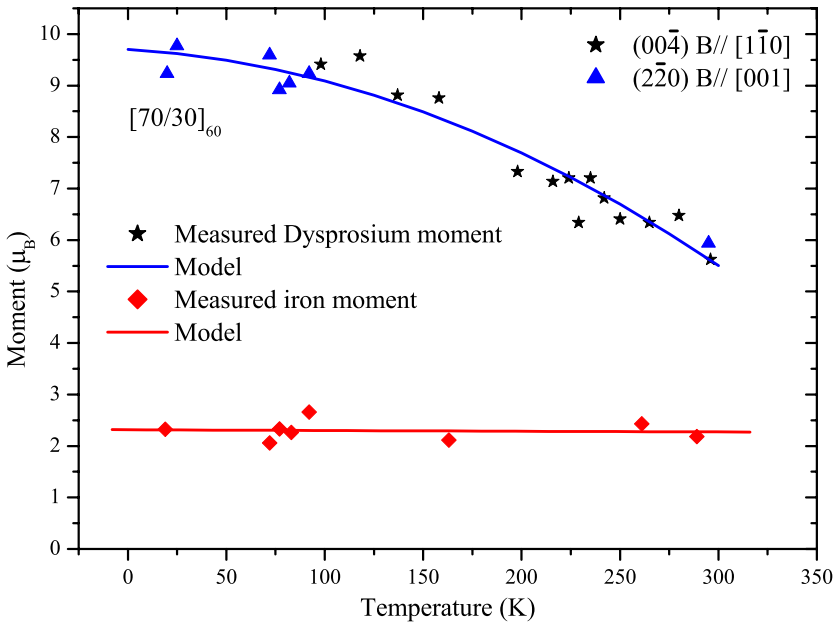

Figure 6. The temperature dependence of the dysprosium and iron moments deduced from the neutron scattering data for sample SL989 of structure $[70/30]_{60}$. The line shows a three-parameter curve fitted to the experimental data.

figure 6. The moments on the Fe atoms, μ_2, were obtained from the data for the $(1\bar{1}\bar{1})$ reflection using

$$\sqrt{2}c_1\mu_1 f_1 - 2\mu_2 f_2 = \sqrt{\frac{3I_M}{2 \times 0.073R}} \tag{10}$$

where $R = 6.8$, and the 3/2 factor arises from the angle between the wavevector transfer and the magnetic moments. The results, figure 6, show that within the errors the moment on the Fe atoms is constant between 10 and 300 K at 2.28 μ_B, while there is a 40% decrease in the Dy moments from 9.8 μ_B at 20 K to about 5.5 μ_B at 300 K. Because the magnetic contributions to the intensities for the reflections $(1\bar{1}\bar{3})$ and $(2\bar{2}\bar{2})$ are small, they were not used to derive values for the moments. The lines on figure 5 indicate the expected intensities based on the moments shown in figure 6 and the results are in good agreement with the experiment.

4.1.3. Magnetic structure with the magnetic field along $[1\bar{1}0]$. The magnetic intensities observed when the magnetic field is applied along the $[1\bar{1}0]$ direction are also shown in figure 5. The structure is more complicated than that found when the field was applied along the [001] direction. We observe substantial magnetic intensity for the $(0\bar{2}0)$ reflection showing that the dysprosium magnetic moments cannot be aligned along the field direction, whereas the intensity for the $(00\bar{4})$ reflection is large. This data were analysed by assuming the structure was a collinear ferrimagnetic structure with the moments perpendicular to the $[00\bar{1}]$ direction. The moments are rotated in the $[1\bar{1}0]$–[110] plane so as to approach the [100] direction but with a tilt toward the $[1\bar{1}0]$ direction to gain Zeeman energy (figure 7). The moment on the iron atoms was assumed to be 2.28 μ_B and the moment on the dysprosium atoms was derived from the intensity of the $(00\bar{4})$ reflection. The results are shown in figure 6. The agreement with the moment magnitude obtained from the $(2\bar{2}0)$ reflection with the field along the [001]

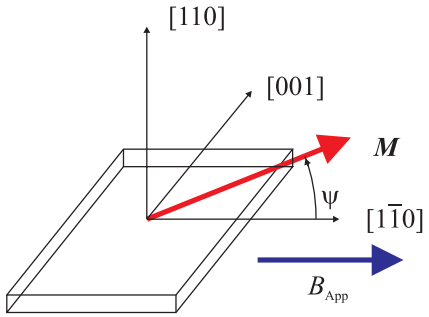

Figure 7. The direction of the moments relative to the film and applied field direction.

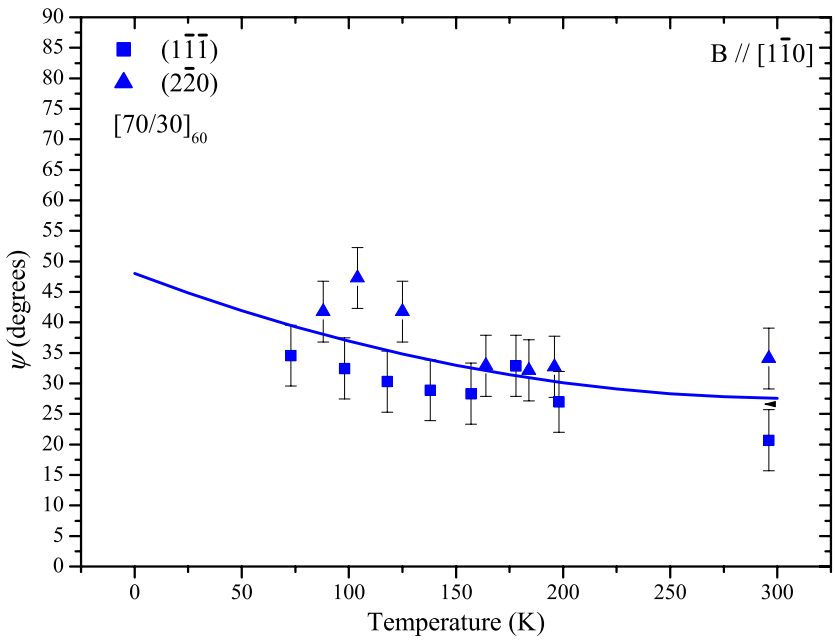

Figure 8. The variation of the out-of-plane angle ψ of the moments as a function of temperature for $\boldsymbol{B} \parallel [1\bar{1}0]$. The solid curve is a three-parameter polynomial fit to the data.

direction shows that the assumptions are correct. We have then found the angle of the moments, ψ, in the (001) plane from the intensities measured for the (2$\bar{2}$0) and (1$\bar{1}\bar{1}$) reflections. The results for ψ, the angle between the moments and the [1$\bar{1}$0] direction, are shown in figure 8. The agreement between the results for the two reflections confirms that the model gives a reasonable description of the structure. The angle increases with cooling presumably because of the increasing anisotropy and at low temperatures tends to 45° allowing the moments to point along the easy out-of-plane [100] direction.

4.1.4. Metastability. Measurements were made by cooling the sample down to 4 K in a field aligned along the [00$\bar{1}$] direction and then rotating the field at low temperatures to the [1$\bar{1}$0] direction. It was found that the structure did not change as the field was rotated. On warming, the structure was unchanged up to about 60 K, but by 80 K it had become very similar to that

obtained by cooling with the field in the $[1\bar{1}0]$ direction. Thus a large spin rotation from $[00\bar{1}]$ to $[1\bar{1}0]$ had taken place. Metastability is therefore important only below 80 K.

4.2. The exchange spring structure of SL1003: $[150/100]_{50}$

4.2.1. Magnetization. The magnetization was measured for the sample SL1003 for two in-plane applied field directions, $[1\bar{1}0]$ and [001], and the results of these measurements are shown in figure 9. The measurements were performed using a Quantum Design MPMS SQUID magnetometer, and each sample was field cooled in (+7 T) to the appropriate temperature before the hysteresis curve was measured. The magnetization has been corrected for a linear paramagnetic contribution to allow for the substrate by estimating where the magnetization measurements had saturated from the high-field data so that the gradient of the paramagnetic contribution could be obtained. The sample area was measured and the thickness was known accurately from the x-ray scattering data, so the number of formula units of RFe_2 could be calculated to obtain the magnetization per formula unit. Although the accuracy of the SQUID is better than 1%, this conversion of the magnetic moment into the average magnetic moment per formula unit introduces a systematic error of up to 10%, due to the difficulty of measuring the sample area. The results show that the magnetization curves for the two different applied field directions are similar, showing that there is not a very well defined 'easy' direction of magnetization for this sample.

The magnetization curves for 300 K, shown in figures 9(a) and (b), suggest that the critical field for reversing the magnetization of the hard $DyFe_2$ blocks is about 0.5 T and that the magnetization of the ferrimagnetic phase is about 1.2 μ_B for each formula unit. On increasing the applied magnetic field the magnetization increases to about 1.8 μ_B. This is qualitatively consistent with the behaviour expected if the magnetization of the Dy atoms is about 7.6 μ_B and that on the Fe atoms is 2.3 μ_B as found above. On increasing the magnetic field an exchange spring structure is formed in the YFe_2 layer, so the net magnetic moment of these layers is close to zero.

The results for the magnetization at 100 K are similar except that the critical fields have increased to about 2.52 T and that the magnetization at low field is about 2.0 μ_B and at high field is about 2.8 μ_B. These results are consistent with a similar model if the moment on the Dy atoms is increased to 9.3 μ_B. The agreement of the model and data is very satisfactory but we could not distinguish between different domains in the sample.

Finally it should be noted that there is a kink in the magnetization curves around $B = 0$ at all temperatures. It has been suggested that this arises from contamination of the sample during cutting, or from non-epitaxial layers in the sample, or from misorientation of the sample [9]. Another possibility is that because the final YFe_2 layer of the superlattice is not tied by a subsequent $DyFe_2$ layer, the iron moments far away from the $DyFe_2$–YFe_2 interface in the YFe_2 layer are free to rotate parallel to the applied field, since this layer is magnetically soft. This results in a magnetic soliton-like behaviour [28] for the rotation of the iron moments in the layer and gives rise to a kink in the magnetization close to zero applied field.

4.2.2. Neutron scattering measurements. For these experiments the $[150/100]_{50}$ sample, SL1003, was aligned with the $(1\bar{1}0)$ crystallographic plane in the scattering plane and the magnetic field was applied vertically in the $[1\bar{1}0]$ direction, figure 4(b). This configuration was chosen because a large 6.5 T field could be applied with the vertical magnet, and because the scattering plane contained the growth direction, so the superlattice satellite peaks could be observed. The intensity of scattered neutrons observed when the wavevector transfer was varied longitudinally, along the [110] growth axis, through the (220) and $(11\bar{1})$ reflections, is shown

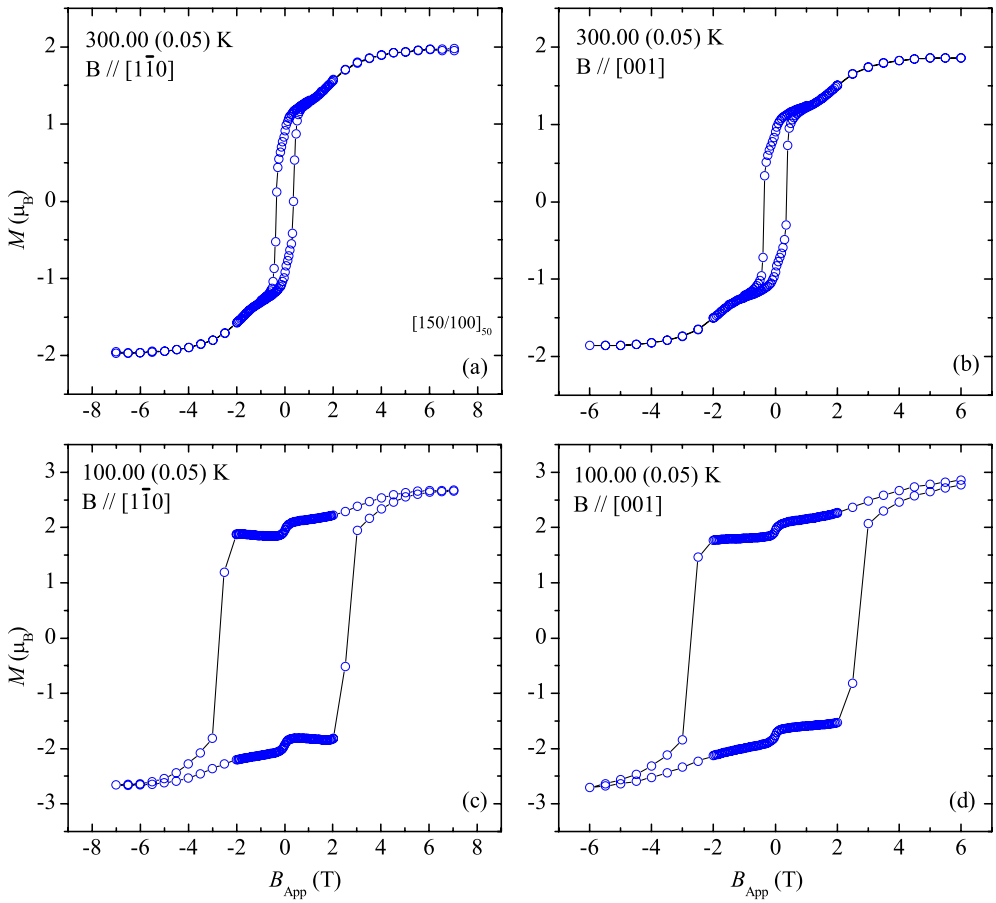

Figure 9. Selected magnetization measurements performed using a SQUID for two temperatures and two field directions for sample SL1003 (150 Å $DyFe_2$)/(100 Å YFe_2)$_{50}$. The units of magnetization are per average formula unit $Dy_{0.6}Y_{0.4}Fe_2$.

in figures 10–12 for three different temperatures, 4.3, 78, and 302 K both in zero field and in an applied field of 6.5 T. The sample was field cooled in +6.5 T before each measurement was made and the different domains could not be identified with unpolarized neutrons. Both reflections have several superlattice peaks confirming the high degree of modulation of the sample. The superlattice peaks do not coincide because they depend differently on the dysprosium and iron structure. Because we have performed unpolarized neutron scattering measurements, the intensities shown in these figures contain both nuclear and magnetic scattering. For a ferrimagnetic structure, the ratios of the magnetic to nuclear scattering for the (220) and (11$\bar{1}$) Bragg reflections are 1.7/1 and 17 000/1 respectively. The (11$\bar{1}$) reflection is very sensitive to the magnetic structure while the (220) reflection is only sensitive to the Dy ions.

The results show that the scattering observed for the (220) reflection is independent of the magnetic field strength. This shows that the field does not change the magnitude or direction of the Dy moments. In contrast the application of the field changes the profile of the (11$\bar{1}$) reflection. With increasing field the largest peak decreases while the satellite peaks increase. This is qualitatively consistent with the structure being a ferrimagnet for zero field and an exchange spring when the field is 6.5 T since we expect a rotation of the iron moment in the

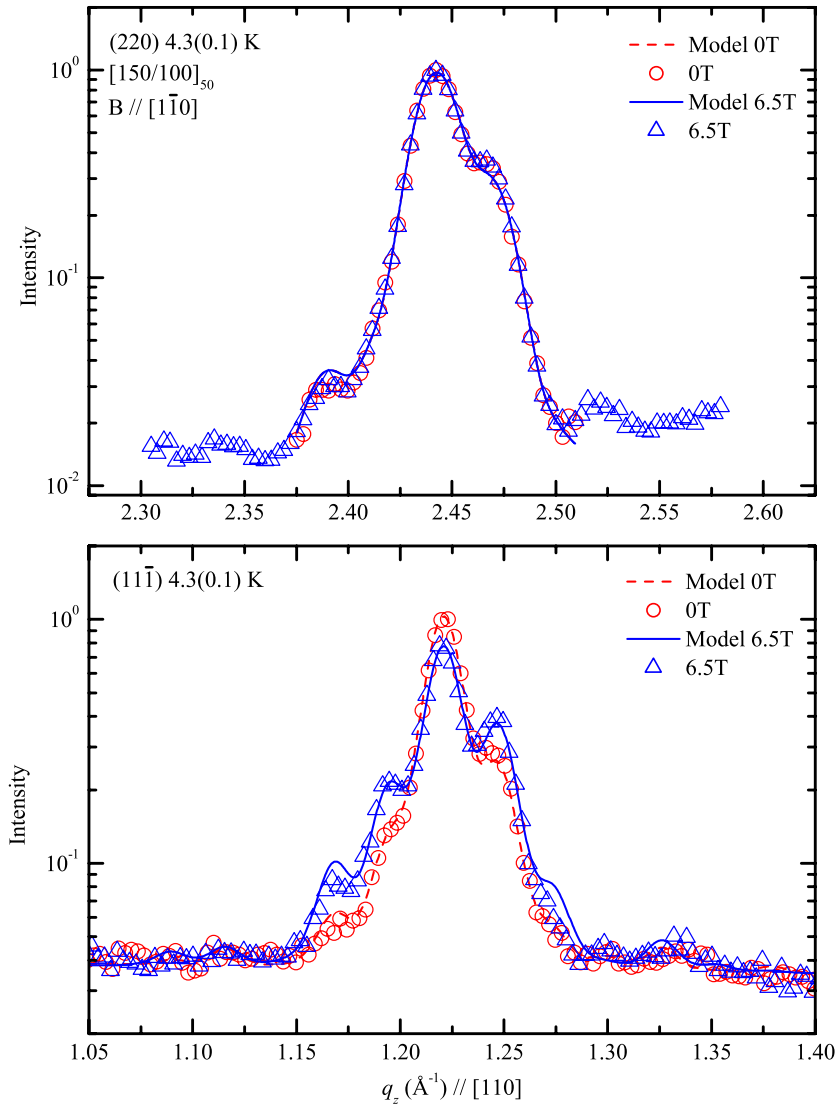

Figure 10. The intensity of scattered neutrons observed when the wavevector transfer was varied longitudinally through two Bragg reflections, at a temperature of 4.3 K, and for two different magnetic fields. The solid and dashed curves are fits of the experimental data to an exchange spring model described in the text. The wavevector component along the bilayer modulation direction is q_z.

YFe_2 layer. The exchange spring structure reduces the average iron moment for each YFe_2 layer, thus decreasing the intensity of the main peak while enhancing the scattering contrast between the two components of the superlattice.

We can show that the results support the existence of an exchange spring structure by performing a quantitative analysis with a more detailed model for both the nuclear and magnetic scattering. For the nuclear scattering we have used the same model as already used to analyse our x-ray scattering measurements. The model describes each layer by lattice parameters, d_1 and d_2, and a number of planes n_1 and n_2. The interfaces have widths λ_1 for the concentration

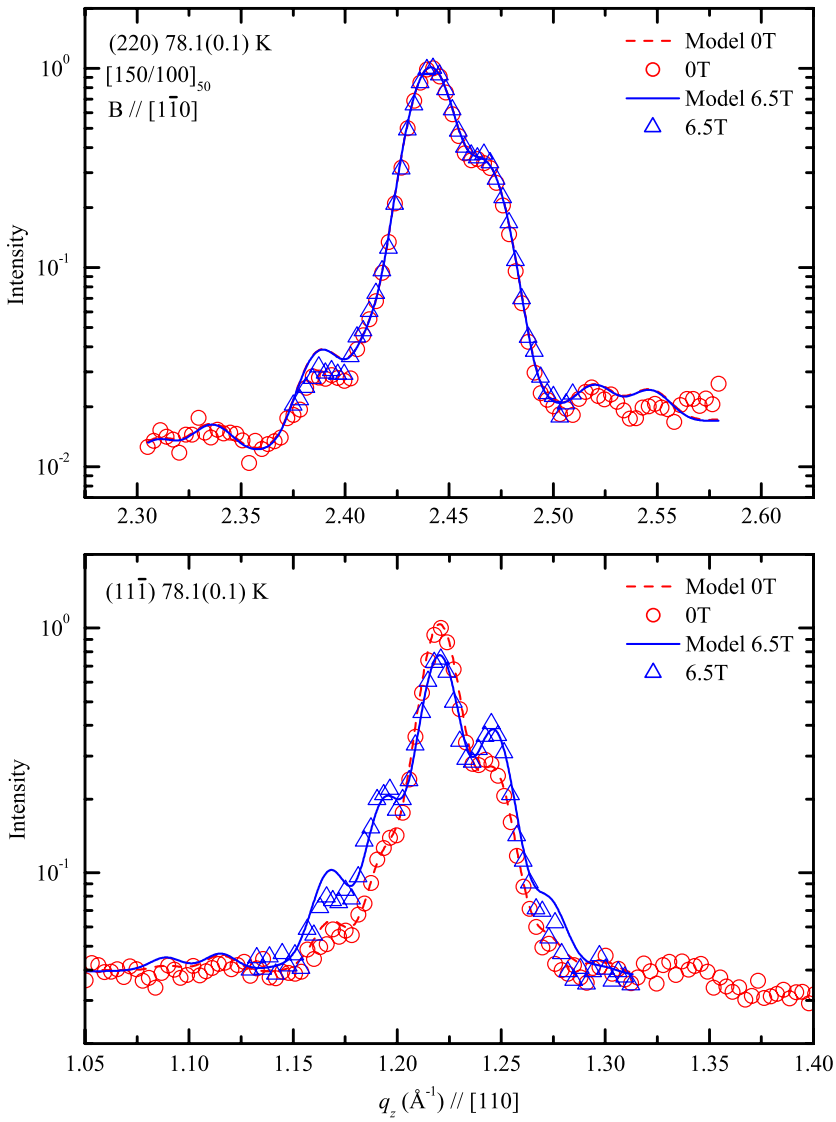

Figure 11. The intensity of scattered neutrons observed when the wavevector transfer was varied longitudinally through two Bragg reflections, at a temperature of 78.1 K, and for two different magnetic fields. The solid and dashed curves are fits of the experimental data to an exchange spring model described in the text. The wavevector component along the bilayer modulation direction is q_z.

and λ_2 for the strain. For the fits to the neutron profile at 300 K all of the parameters were held fixed at the values determined by the x-ray measurements, while for the fits for 80 and 4 K the lattice parameters and the interface width of the strain were allowed to vary. At zero field the magnetic structure was assumed to be ferrimagnetic, while in the 6.5 T field, the exchange spring structure, described in section 3.3, was fitted to the data. The magnetic moments on the Fe atoms were assumed to be independent of temperature with a magnitude of 1.77 μ_B [29] as found in YFe_2, while the moment on the Dy atoms was fitted to the data at a temperature of 300 K but held constant at 10.0 μ_B for the fits at lower temperatures. Although the value

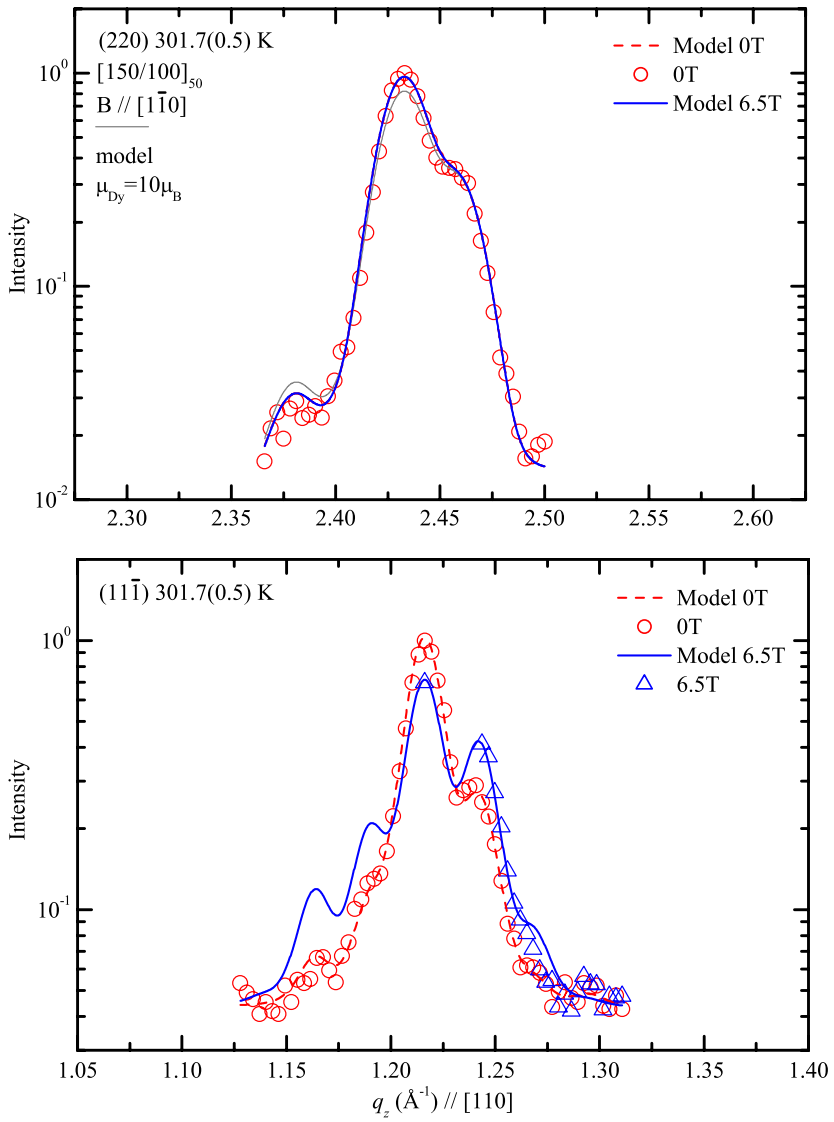

Figure 12. The intensity of scattered neutrons observed when the wavevector transfer was varied longitudinally through two Bragg reflections, at a temperature of 302 K, and for two different magnetic fields. The solid and dashed curves are fits of the experimental data to an exchange spring model described in the text. The wavevector component along the bilayer modulation direction is q_z.

used for the magnitude of the moment on the iron site is somewhat smaller than the value used for the analysis of the other samples, the values are consistent within reasonable error, since the absolute intensities for the (11$\bar{1}$) reflection of the model and data were not compared. The model scattering was then convoluted with a Gaussian experimental resolution, scaled by an adjustable scaling factor, and linear background parameters were fitted to the profiles in zero magnetic field. The results of the fits are shown in figures 10–12, and there is clearly excellent agreement.

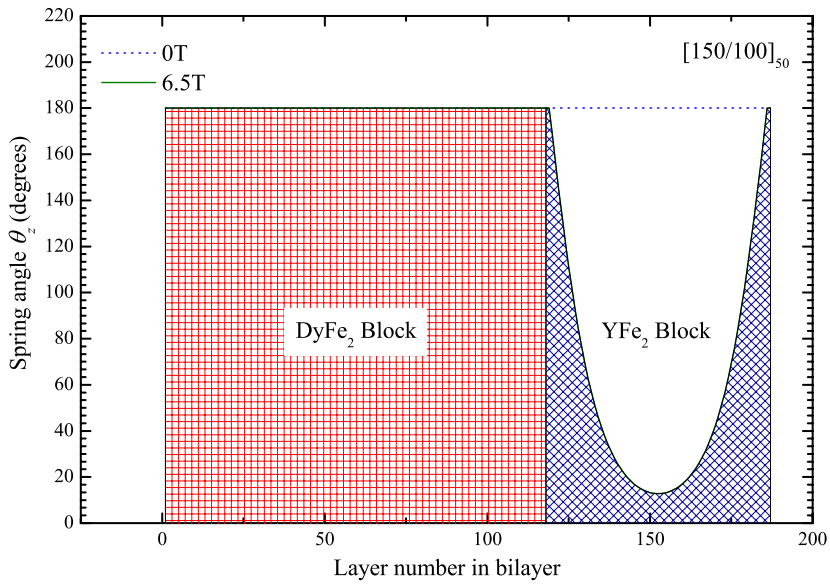

Figure 13. The rotation of the iron moments as a function of layer number of the (110) layers for the fitted data obtained using an exchange spring model described in the text.

Table 3. The structural parameters of sample SL1003 [150 Å $DyFe_2$/100 Å $YFe_2]_{50}$ determined by neutron scattering at three different temperatures. The parameters given in the table were obtained from simultaneous fits of two measured diffraction profiles by the model described in section 3. d_1 and d_2 are the mean lattice parameters of the $DyFe_2$ and YFe_2 blocks in the superlattice, and λ_1 and λ_2 are the concentration and strain profile widths, in units of layers.

Temperature (K)	d_1 (Å)	d_2 (Å)	λ_1	λ_2
4.3(0.1)	7.259(0.001)	7.306(0.002)	15(6)	1(2)
78.1(0.1)	7.260(0.002)	7.313(0.005)	15(6)	2(2)
301.7(0.5)	7.280(0.001)	7.349(0.001)	15(6)	15(2)

The structural parameters in table 3 show that on cooling from room temperature, the sample undergoes a thermal contraction of 0.29%. More unexpected is the decrease in the width of the interface in the strain from 15 to 2 lattice parameters at low temperature. In part this occurs because the YFe_2 layer contracts faster than the $DyFe_2$ layer (by 0.02 Å), so the lattice constant mismatch at the interface is almost halved at low temperatures.

In zero magnetic field we find that the magnetic structure is the ferrimagnetic structure of figure 1(a) and that the moment on the Dy atoms at 302 K is reduced from the low-temperature value of 10 to 6.0(0.4) μ_B in agreement with the temperature dependence for the $[70/30]_{60}$ sample deduced in the previous section, as shown in figure 6.

The magnetic structure in an applied field of 6.5 T was calculated from the exchange spring model as described in section 3.3 with the value for the bending field, $B_B \simeq 1.5$ T, determined from equation (8), and the angles of the magnetic moments were calculated and the results are shown in figure (13). The model assumes that in the $DyFe_2$ layer all the dysprosium moments are parallel to the applied field and all the iron moments are antiparallel, while the moments in the YFe_2 rotate from antiparallel throughout the layer by an amount determined from experiment via the spring model. The magnetic scattering was then calculated and added

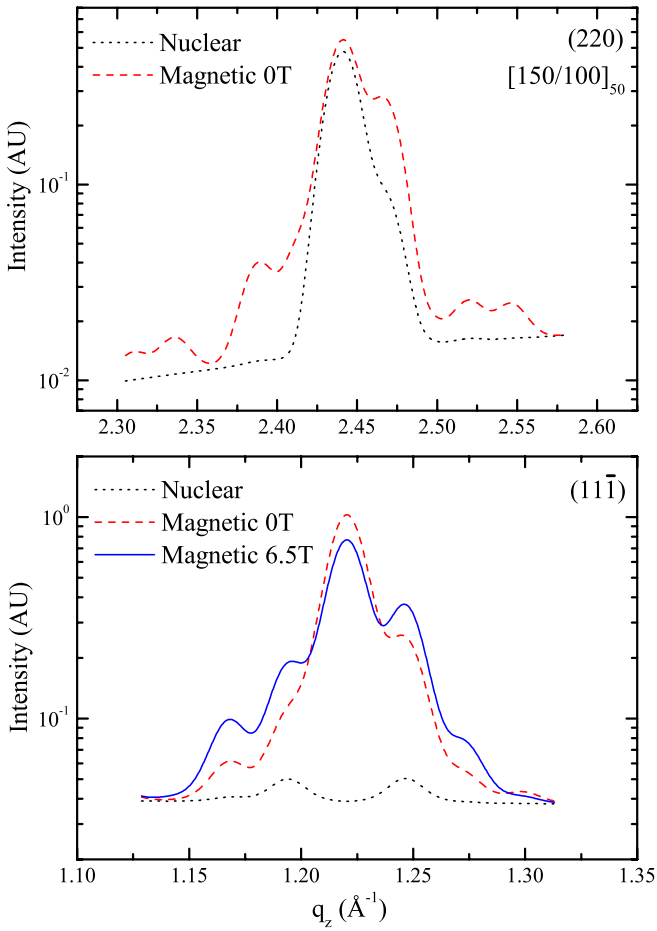

Figure 14. The calculated nuclear and magnetic contributions to the observed scattered intensity for two Bragg reflections as a function of applied magnetic field at 80 K. For the (220) reflection, the magnetic scattering from the structure with an applied magnetic field of 6.5 and 0 T are indistinguishable.

to the nuclear scattering to give the total scattering. It is compared with the experimental results for the three temperatures shown in figures 10–12. The individual calculated magnetic and nuclear contributions are shown at 80 K in figure 14. The results for the (220) reflection show that the magnetic scattering is independent of the magnetic field. Figure 14 shows that the magnetic and nuclear components are of comparable size but that the superlattice satellites arise largely from the magnetic scattering. This is because there is more relative difference between the dysprosium and yttrium magnetic moments than between their coherent neutron scattering lengths. The results for the (11$\bar{1}$) reflection show that the scattering is largely magnetic although the nuclear scattering has the unusual feature that the superlattice satellites are larger than the main Bragg peak. Our fitted model for the magnetic scattering clearly shows that in a field the spring exchange structure gives less intensity for the main peak and more for the satellites than the ferrimagnetic structure. The good agreement between the calculations and the observations, particularly given that no new parameters were introduced, shows that the exchange spring structure is indeed a good description of the magnetic structure of this superlattice in a field of 6.5 T as suggested by the magnetization measurements.

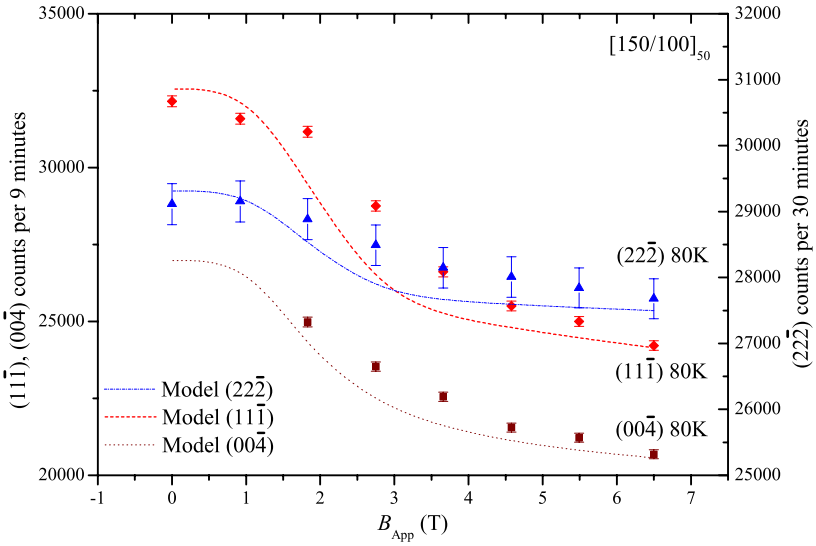

Figure 15. The intensity as a function of applied magnetic field for several reflections. The intensity observed for the (00$\bar{4}$) and (11$\bar{1}$) reflections arises from contributions from all the atoms in the structure, while the intensity observed for the (22$\bar{2}$) reflection arises purely from the iron atoms. The right-hand axis is the intensity scale for this reflection. The curves are the changes in intensity predicted by the exchange spring model described in section 3.

In order to investigate further the effect of a magnetic field on the magnetic structure, the intensities of the (11$\bar{1}$), (22$\bar{2}$), and (00$\bar{4}$) reflections were measured as a function of applied magnetic field. The measurements were made at a temperature of 80 K where most moments are aligned and the system does not exhibit appreciable hysteresis. The maximum ratios of the magnetic to nuclear scattering for these reflections are 17 000, 0.18, and 26 respectively. The scattering from the (22$\bar{2}$) peak is due to the iron atoms alone but unfortunately its low magnetic/nuclear ratio means that any change in the magnetic scattering will give only a small change in the intensity. Nonetheless this change was detected with a counting time of 30 min/point (figure 15 right-hand axis). Figure 15 (left-hand axis) also shows the results for the (11$\bar{1}$) and (00$\bar{4}$) reflections measured at 9 min/point. For all three reflections there is a similar decrease in the intensity with increasing magnetic field. The intensities were also calculated using the exchange spring model, the lines in figure 15, and show that the model gives a reasonable description of the measurements. The disagreement is largest for magnetic fields of about 3 T and would be reduced if the bending field was larger.

This discrepancy between the model and the data could be due to the oversimplification of the exchange spring model in assuming that the anisotropy of the hard layer is much greater than that of the soft layer. This assumption results in the exchange spring being confined to the magnetically 'soft' YFe_2 layers in the superlattice. The results show that the exchange spring model in which the spring is confined to the YFe_2 layers does not describe well the data for fields near the bending field. This is probably due to considerable exchange spring penetration into the magnetically 'hard' $DyFe_2$ layers.

4.3. Spin-flop structures in SL990: $[50/70]_{60}$

4.3.1. Preliminaries. Sample SL990 was aligned in the horizontal magnetic field magnet with the (110) growth plane in the scattering plane, figure 4(a), as with the experiments discussed

in section 4.1 for SL989. The intensities of the $(00\bar{4})$, $(1\bar{1}\bar{3})$, $(2\bar{2}\bar{2})$, $(1\bar{1}\bar{1})$, and $(2\bar{2}0)$ Bragg reflections were measured as a function of temperature, and magnetic fields were applied mostly along either the [001] or $[1\bar{1}0]$ direction. The data analysis to obtain the nuclear and magnetic components of the scattering, and hence the squares of the structure factors, was initially performed as for SL989. The results for the magnetic scattering in figure 16 show that the $(2\bar{2}0)$ and $(1\bar{1}\bar{1})$ reflections are largely independent of the direction of the magnetic field. The intensity observed for the $(00\bar{4})$ Bragg reflection is larger with the field applied parallel to the [001] direction than when the field was along the $[1\bar{1}0]$ direction. The results then clearly show that the moment direction is not parallel to the applied field and so the method used above to determine the nuclear component cannot be used for this sample. The method adopted was to compare the maximum intensity observed for each reflection with the sum of the structure factors squared, calculated assuming that the moment direction was perpendicular to the wavevector transfer, $\boldsymbol{Q}$. The results are summarized in table 4 and show that the R-ratio is close to 1.61 for the $(00\bar{4})$, $(1\bar{1}\bar{3})$, and $(2\bar{2}0)$ reflections, is 2.97 for $(2\bar{2}\bar{2})$, and is 1.41 for $(1\bar{1}\bar{1})$. The $(1\bar{1}\bar{1})$ intensity is dominated by the magnetic contribution and so R could be smaller if the moment was not perpendicular to the wavevector transfer. We have therefore analysed the data assuming $R = 1.61$. The only exception is the data for the $(2\bar{2}\bar{2})$ reflection that are dominated by the nuclear scattering. We have failed to identify the origin of the extra scattering for this reflection and so these results were not used in the subsequent analysis. The magnetic intensities shown in figure 16 were then obtained by subtracting from the total scattering the nuclear scattering using the calculated structure factors and $R = 1.61$.

4.3.2. The structure with the field applied along [001]. The magnetic scattering has been analysed assuming that the structure is similar to the collinear ferrimagnetic structure shown in figure 1(a). When the field is applied along the [001] direction at low temperatures, the magnetic intensities, figure 16, are close to the theoretical maximum intensities for both the $(00\bar{4})$ and $(2\bar{2}0)$ reflections. The moment direction must then be at least approximately perpendicular to both of these wavevectors namely along the [110] growth direction. We have therefore assumed this direction for the dysprosium moments and that all iron moments are antiparallel with a magnitude of 2.28 μ_B. We could then determine the moment on the dysprosium atoms from the observed scattered intensity and these are shown by the lines in figure 16 along with the resulting moments in figure 17. The similarity, particularly at low temperatures, of the moments deduced from reflections with widely different structure factors, and the general agreement with the results for $[70/30]_{60}$ in figure 6, strongly support our deduction that the moments adopt a spin-flop direction perpendicular to the applied field.

At high temperatures μ_{Dy} determined from the $(1\bar{1}\bar{1})$ reflection is significantly below the other data. Since $\boldsymbol{B} \parallel [001]$ this suggests that the moments are tilting away from [110] with a component along $[1\bar{1}\bar{1}]$. Probably this means that the model that we have used is too simple.

4.3.3. Magnetization measurements. The magnetization was measured with the field applied along the [001] direction using the same techniques as described in section 4.2.1, and the results are shown in figure 18.

The results for $[50/70]_{60}$ are very different from those shown in figure 9 especially at 300 K. The $[150/100]_{50}$ sample had a magnetization of over 1 μ_B in a field of 1 T, whereas for $[50/70]_{60}$ the magnetization increases more slowly. In a field of 6 T it is still less than 1 μ_B and increasing. This is consistent with the structures being very different and for the moments being aligned perpendicular to the field for $[50/70]_{60}$. At lower temperatures the

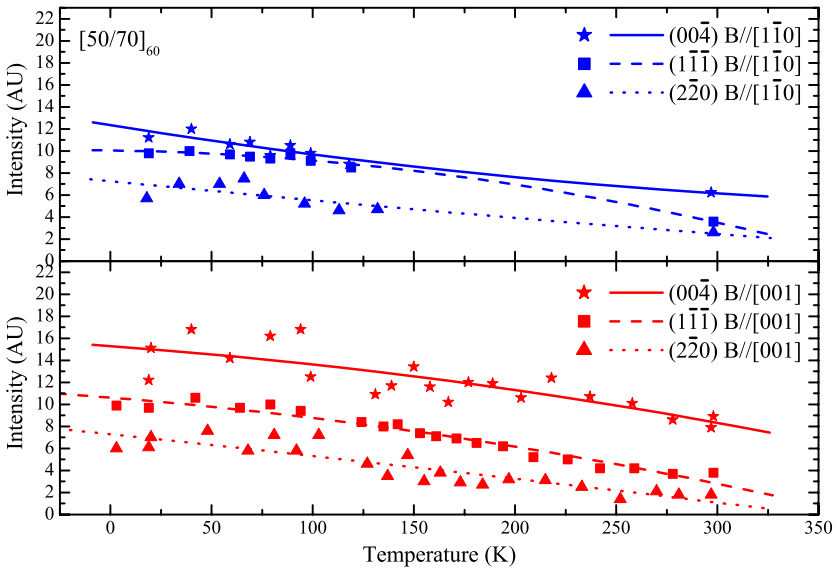

Figure 16. The resolution-corrected intensities of the measured reflections of SL990 $[50/70]_{60}$ as a function of temperature for two applied field directions. The curves are a guide to the eye.

Table 4. The nuclear and magnetic scattering for SL990 $[50/70]_{60}$. The intensity (structure factor squared) is calculated for the nuclear and maximum magnetic intensity $\boldsymbol{M} \perp \boldsymbol{Q}$ to give the total maximum intensity. The maximum observed scattering is divided by this to give the ratio R. $\mu_1 = 9.8\ \mu_B$ and $\mu_2 = 2.28\ \mu_B$.

Reflection	Calculated nuclear scattering	Calculated magnetic scattering	Total scattering	Maximum observed scattering	Ratio R
(00$\bar{4}$)	2.04	10.27	12.31	19.8	1.61
(1$\bar{1}\bar{3}$)	12.62	0.49	13.01	21.2	1.62
(1$\bar{1}\bar{1}$)	0.05	7.47	7.52	10.5	1.41
(2$\bar{2}\bar{2}$)	14.29	2.22	11.51	49.0	2.97
(2$\bar{2}$0)	5.54	4.68	10.22	16.2	1.59

magnetization develops a hysteresis loop but the magnetization for $B < 6$ T is less than 1 μ_B, in contrast to the results obtained for $[150/100]_{50}$. It is unclear how the magnetization is related to the structure determined by neutron scattering where the sample was cooled in a lower field.

4.3.4. The structure with the field applied along [1$\bar{1}$0]. The main difference when the field was applied in the [1$\bar{1}$0] direction instead of the [001] direction was a decrease in the intensity of the (00$\bar{4}$) reflection, figure 16. This indicates that the moments are tilted towards the [001] direction from the [110] growth direction found in section 4.3.2, as shown in figure 19. The angle of deviation, ψ, was found by comparing the intensities for $\boldsymbol{B} \parallel$ [1$\bar{1}$0] of the reflections with those calculated for $\boldsymbol{B} \parallel$ [001] in section 4.3.2, but with the dysprosium moments held at the average value of μ_{Dy} shown in figure 17. The results for the (2$\bar{2}$0) reflection showed that on average the ratio of the intensities for the two applied field directions was 1.005(0.035) showing that the tilting of the moments is likely in the (1$\bar{1}$0) plane. The tilting angle deduced

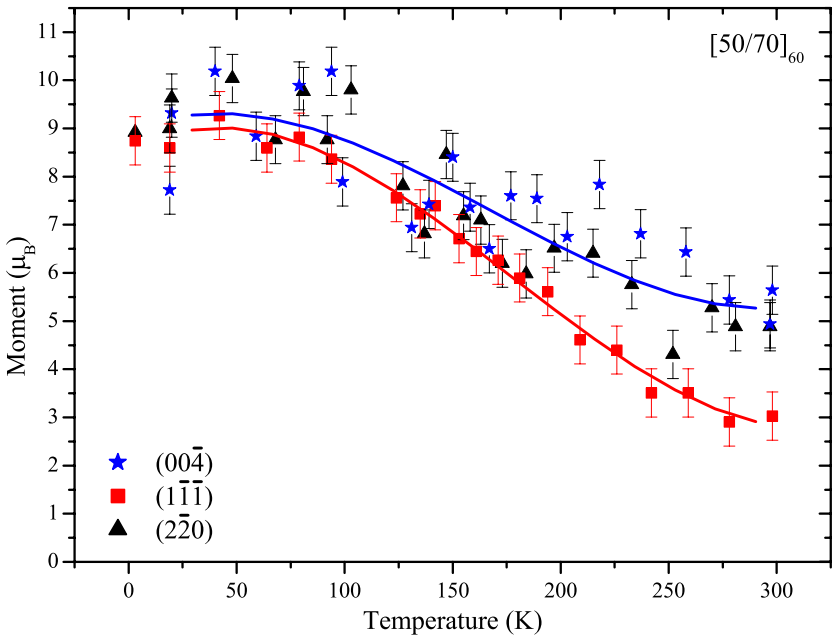

Figure 17. The temperature dependence of the dysprosium moment deduced from the neutron scattering for different reflections. The upper solid curve is a guide to the eye for the (00$\bar{4}$) and (2$\bar{2}$0) data and the lower line is for the (1$\bar{1}\bar{1}$) data.

from the (00$\bar{4}$) and (1$\bar{1}\bar{1}$) reflections is shown in figure 20. The angle deduced from the (00$\bar{4}$) reflection is somewhat larger than that from the (1$\bar{1}\bar{1}$) reflection probably because the model of the structure is too simple. On average, however, the tilting is about 28° away from the [110] direction towards the [001] direction.

A better understanding of these results can be obtained from consideration of an oversimplified model of a ferrimagnet in an applied field. We consider a linear chain consisting of alternate components with moments M_1 and M_2 representing the net moments/unit area of each of the layers of the superlattice. These are coupled by a Heisenberg exchange interaction, J, and a field $\boldsymbol{B}$ is applied along the z-axis. The Hamiltonian is given by

$$H = J\boldsymbol{M}_1 \cdot \boldsymbol{M}_2 - B(M_1(z) + M_2(z)). \tag{11}$$

The lowest-energy solutions were obtained in terms of the ratio of the fixed length moments $r = M_1/M_2$ and the reduced field $b = B/[J\sqrt{|M_1 M_2|}]$ and the phase diagram is illustrated in figure 21. There are three phases corresponding to the fully aligned ferrimagnetic phase at low fields of figure 1(a), the fully aligned phase of figure 1(d) and an intermediate canted phase similar to the spin-flop phase of an antiferromagnet. As the moments become nearly equal, $r = 1$, the phase boundary line between the ferromagnetic phase and the spin-flop phase occurs at smaller and smaller fields. The angles of the moments away from the z-axis are shown in figure 22 as a function of b for $r = 1.05$. The ferrimagnetic phase has the larger moment aligned along the field direction $\theta_1 = 0$ and the smaller moment aligned antiparallel. On crossing the phase boundary by increasing b the smaller moment swings round to alignment with the field whereas the larger moment cants away from the field at first and then reverts back to alignment with the field. The extent of swing away from thee field direction increases as r becomes closer to 1 and reaches $-90°$ for $r = 1$.

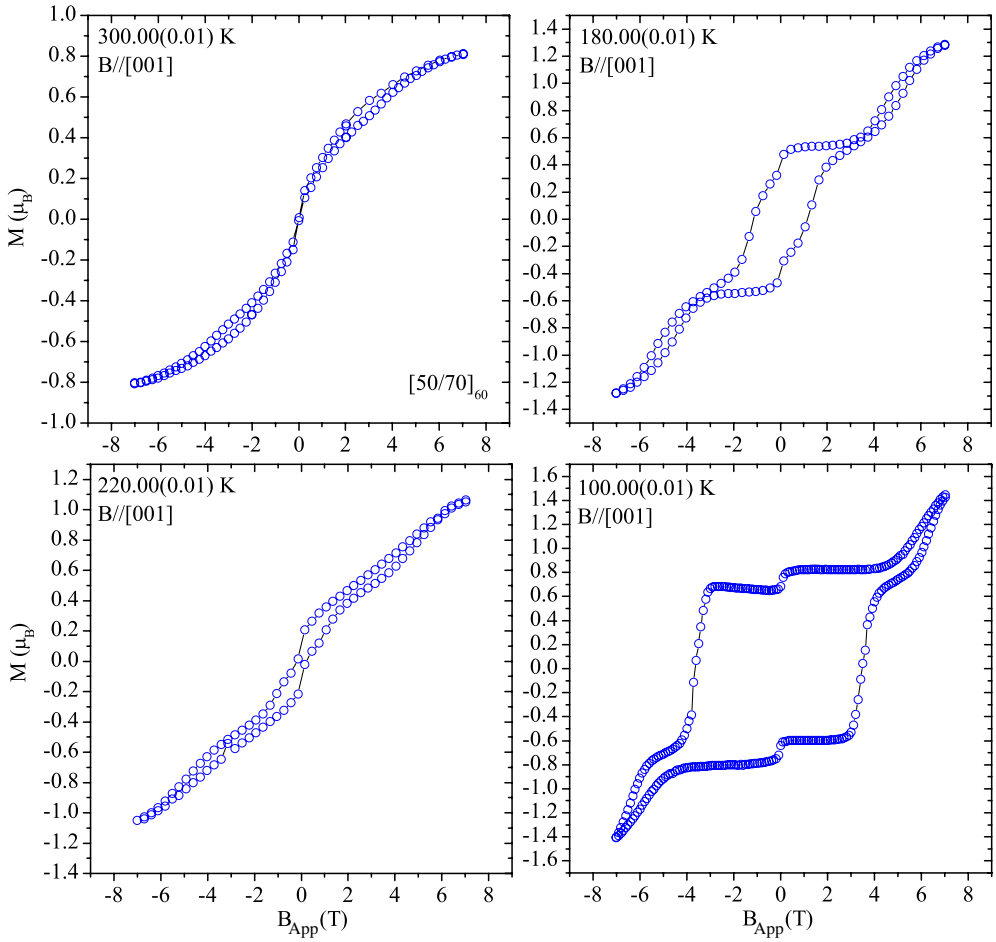

Figure 18. The average magnetization in μ_B per formula unit obtained using a SQUID for sample SL990 $[50/70]_{60}$ with the field applied along the [001] direction.

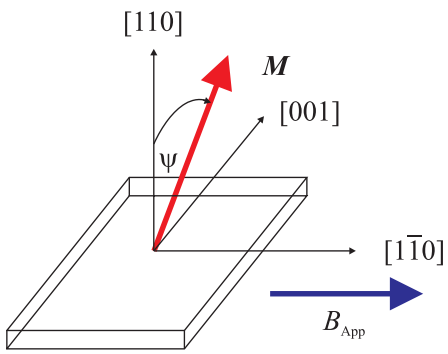

Figure 19. The direction of the moments relative to the film and applied field direction.

As the temperature of our samples is varied the moment on the dysprosium atoms changes and so both r and b change and the sample will move on a trajectory in the phase diagram.

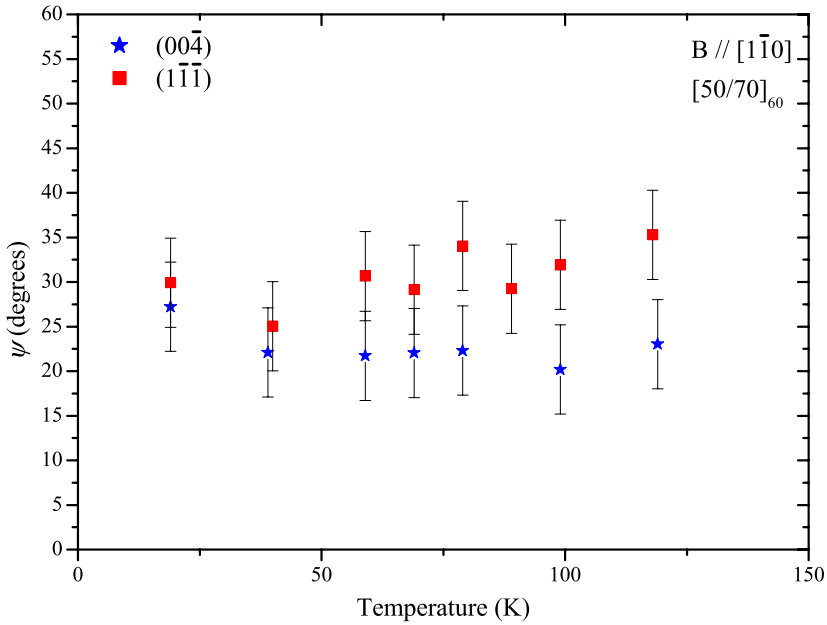

Figure 20. The variation of the tilt angle ψ from the [110] direction of the moments towards the [001] direction as a function of temperature for $\boldsymbol{B} \parallel [1\bar{1}0]$.

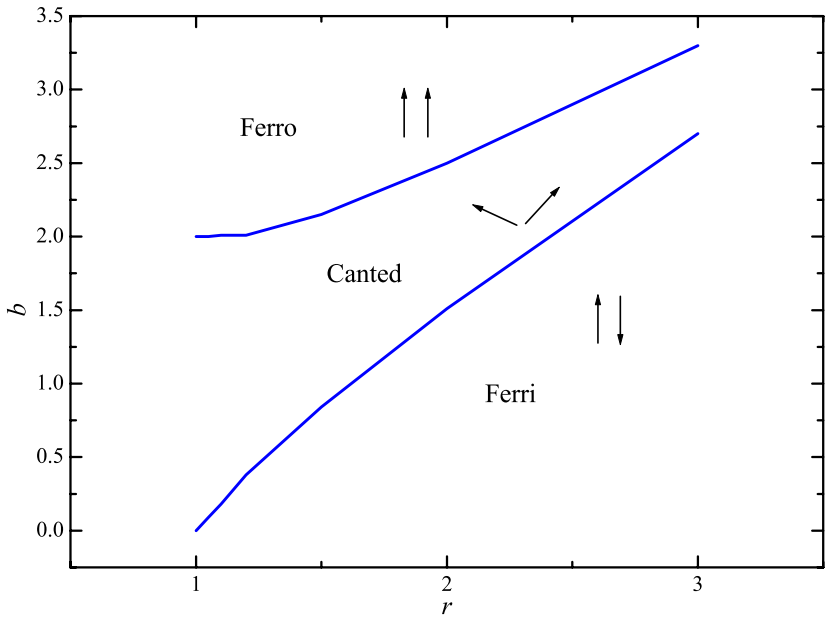

Figure 21. The phase diagram of a ferrimagnet in an applied field as a function of applied field $b = B/[J\sqrt{(M_1 M_2)}]$ and the ratio of the moments $r = M_1/M_2$. The arrows show schematically the direction of the moments in the layers for the three phases.

Nevertheless it is clear that the interesting region is close to the phase boundary of the ferromagnetic and canted phases and this occurs at low field for samples in which the net

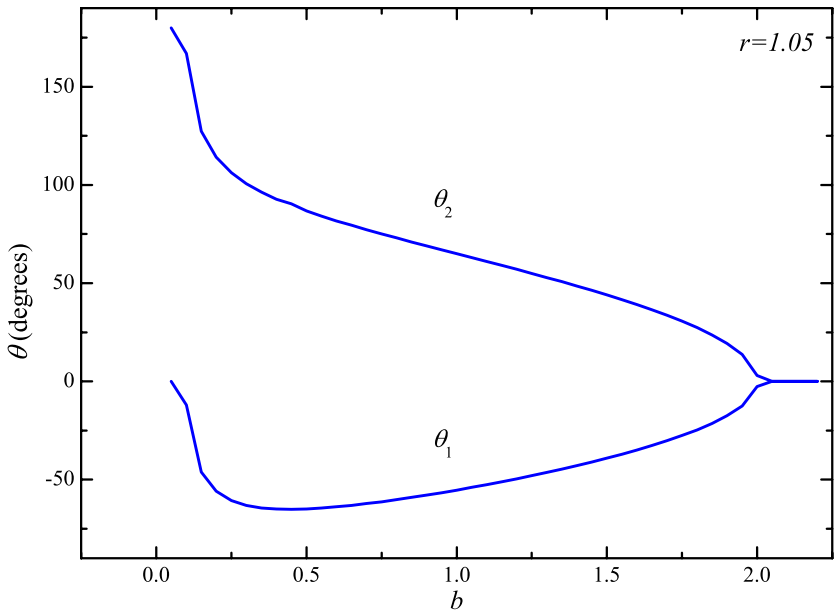

Figure 22. The angles of the moments of a ferrimagnet in an applied field, b, for the largest moment θ_1 and the smallest moment θ_2. $r = M_1/M_2 = 1.05$.

moment of the two layers is close. For our samples the $DyFe_2$ layer always has the largest total moment for SL989 $[70/30]_{60}$, whereas for SL990 $[50/70]_{60}$ the two layers have the same moment at low temperature but it is substantially different at higher temperature. It is then possibly surprising that the structures observed and described in section 4.3 are not more temperature dependent. Our results suggest that sample SL990 $[50/70]_{60}$ has almost equal moments on the two layers at about 200 K. We plan to study the behaviour near this temperature in more detail.

The model described above cannot be expected to describe the different phases of the superlattices in detail. It assumes that the moments in each layer are strongly coupled while the exchange interactions between the layers are relatively weak. In the superlattices, the exchange constants are approximately the same. However, we have shown that for superlattices where the net moment of the $DyFe_2$ and YFe_2 layers are similar, a spin-flop structure is adopted by the moments in these layers.

5. Conclusions and discussion

We have used neutron scattering to determine the magnetic structures of three different $DyFe_2$–YFe_2 superlattices. Although the measurements were difficult because both materials have ferromagnetic structures, we have succeeded in separating the magnetic scattering from the nuclear scattering. Since an earlier attempt with polarized neutron beams was unsuccessful, we have used unpolarized neutrons with the aid of both horizontal and vertical magnetic fields to determine the magnetic structure for several field directions and over a wide range of temperature.

The results show that the three superlattices form different structures and so illustrate different aspects of the physics of these superlattices. They serve to establish how the

superlattice properties vary with the thickness of the 'magnetically hard' $DyFe_2$ and 'soft' YFe_2 layers. Sample SL989 had a thick layer of (73 Å) $DyFe_2$ and a thin layer of YFe_2 (24 Å). The $DyFe_2$ layer, whose moment is dominated by that of dysprosium is then expected (section 4.1) to align in a direction that favours both the anisotropy axis and the applied magnetic field direction. The thin YFe_2 layer has a bending field that would overcome the iron–iron exchange that is substantially larger than the fields that we could apply and its net moment is smaller than the net moment of the $DyFe_2$ layer. The iron moments in both layers then align largely antiparallel to the $DyFe_2$ net moment. When the applied field is in the soft [001] direction the moments are parallel to the [001] direction at all temperatures below 300 K. The behaviour is more complex when the field is applied in the $[1\bar{1}0]$ direction. The moment direction is then found to be at an angle between the field direction and the [110] growth direction and close to the 'soft' [100] or [010] directions. Presumably this arises because the Dy crystal field anisotropy favours these directions. We were unable to ascertain whether the moments in successive $DyFe_2$ layers along the growth direction were parallel or antiparallel. The results were consistent with an almost temperature-independent moment on the Fe atoms of 2.28 μ_B that is larger than the values obtained for bulk $DyFe_2$ (1.5 μ_B) and for YFe_2 (1.77 μ_B) [29] but close to the moment on bulk Fe. The ordered moment of the Dy atoms decreases on heating from nearly 10 μ_B at 4 K to about 6 μ_B at 300 K. At low temperature, below 80 K, the moment direction remained fixed under changes in the direction of the 2.6 T magnetic field, but above 80 K the moments could follow changes in the field direction.

Sample SL1003 has thicker YFe_2 layers (88 Å) and so the bending field is reduced to less than the 6.5 T field that could be applied by the vertical field magnet. The layers then distort into a spring structure so as to reduce the Zeeman energy as shown in figure 1(b). Detailed measurements were performed, in fields of 0 and 6.5 T, of the main Bragg peaks and the associated satellite peaks. When the field was increased the intensity of the main Bragg peak decreased while that of the satellite peaks increased as expected qualitatively. A more detailed calculation of the exchange spring structure gives very good agreement with the scattered profiles showing that the structure is understood quantitatively. The detailed field dependence of the structure was somewhat different from the observations and suggests that the bending field is probably somewhat larger than that given by the simple theory.

The results were most surprising for the sample SL990 that had layers with a thickness of 55 Å for the $DyFe_2$ and 67 Å for the YFe_2. The thicknesses are then sufficiently small that the applied field, 2.6 T, is much less than the bending field. The results clearly show that when a magnetic field is applied along the 'soft' [001] direction, the moments are *not* aligned along the applied field but mostly aligned perpendicular along the [110] growth direction. We consider that this occurs because at low temperature the total net moment on the $DyFe_2$ layer is very close to that of the total moment of the YFe_2 layer. The sample is then almost an antiferromagnet and so aligns with the moments perpendicular to the field in a spin-flop phase. When the magnetic field is applied in the $[1\bar{1}0]$ direction the magnetic moments are perpendicular to the magnetic field and tilted about 28° away from the [110] growth axis towards the [001] direction. The ferrimagnetic model used to gain an understanding of the results needs to be improved to incorporate the distortions of the blocks as shown by the success of the exchange spring model for the thicker layers. We plan to investigate a model involving both layer distortions and the canted phases in the future.

Our experiments have shown that $DyFe_2$–YFe_2 superlattices have a rich variety of ferrimagnetic, ferromagnetic, and different intermediate phases. Theses phases depend on the thickness of the layers and require the development of a new theory. If this theory is to be tested, improved neutron scattering experiments are required that measure the intensities of a larger number of Bragg reflections and more adequately separate the nuclear and magnetic

Bragg intensities. The results will, however, provide understanding not only of the ordered magnetic Laves phase superlattices but also of 3d transition metal superlattices of ferromagnetic materials.

Acknowledgments

This work was funded by the UK Engineering and Physical Sciences Research Council (EPSRC) and a grant from the British Council/National Research Council of Canada Cooperative Research Programme. A preliminary measurement was performed at HMI in Berlin and we are grateful to Jens Klenke and Sergei Danilkin for help in this experiment. Ron Donaberger and Andrew Cull provided invaluable technical support at Chalk River. We would also like to thank Graham Bowden for useful discussions.

References

[1] Coey J M D and Skomski R 1993 New magnets from interstitial intermetallics *Phys. Scr.* T **49** 315–21

[2] Gordeev S N, Beaujour J M L, Bowden G J, Rainford B D, de Groot P A J, Ward R C C, Wells M R and Jansen A G M 2001 Giant magnetoresistance by exchange springs in $DyFe_2$–YFe_2 superlattices *Phys. Rev. Lett.* **87** 1–4

[3] Buschow K H J 1977 Intermetallic compounds of rare-earth and 3d transition metals *Rep. Prog. Phys.* **40** 1179–256

[4] Swaddling P P, Cowley R A, Ward R C C and Wells M R 1996 Magnetic structures of holmium–lutetium alloys and superlattices *Phys. Rev.* B **53** 6488–98

[5] Ward R C C, Wells M R, Bryn-Jacobsen C, Cowley R A, Goff J P and McMorrow D F 1996 MBE growth and characterisation of light rare-earth superlattices *Thin Solid Films* **275** 137–9

[6] McMorrow D F, Swaddling P P, Cowley R A, Ward R C C and Wells M R 1993 The chemical structure of rare earth superlattices: a high-resolution x-ray scattering study *J. Phys.: Condens. Matter* **5** 6553–67

[7] Jehan D A, McMorrow D F, Cowley R A, Ward R C C, Wells M R and Hagmann N 1993 Magnetic structure of holmium–yttrium superlattices *Phys. Rev.* B **48** 5594–606

[8] Dumesnil K, Dutheil M, Dufour C and Mangin Ph 2000 Spring magnet behaviour in $DyFe_2$–YFe_2 Laves phase superlattices *Phys. Rev.* B **62** 1136–40

[9] Sawicki M, Bowden G J, de Groot P A J, Rainford B D, Beaujour J M L, Ward R C C and Wells M R 2000 Exchange springs in antiferromagnetically coupled $DyFe_2$–YFe_2 superlattices *Phys. Rev.* B **62** 5817–20

[10] Sawicki M, Bowden G J, de Groot P A J, Rainford B D, Beaujour J M L, Ward R C C and Wells M R 2000 Engineering coercivity in epitaxially grown (110) films of $DyFe_2$–YFe_2 superlattices *Appl. Phys. Lett.* **77** 573–5

[11] Beaujour J M L, Gordeev S N, Bowden G J, de Groot P A J, Rainford B D, Ward R C C and Wells M R 2001 Negative coercivity in epitaxial grown (110) $DyFe_2$–YFe_2 superlattices *Appl. Phys. Lett.* **78** 964–6

[12] Beaujour J M L, Bowden G J, Gordeev S, de Groot P A J, Rainford B D, Ward R C C and Wells M R 2001 Exchange springs in YFe_2 dominated $DyFe_2$–YFe_2 superlattices *J. Magn. Magn. Mater.* **226–230** 1870–2

[13] Gordeev S N, Beaujour J M L, Bowden G J, de Groot P A J, Rainford B D, Ward R C C and Wells M R 2001 Spin configurations and negative coercivity in epitaxially grown $DyFe_2$–YFe_2 superlattices *J. Appl. Phys.* **89** 6828–30

[14] Beaujour J M L, Bowden G J, Gordeev S, de Groot P A J, Rainford B D, Sawicki M, Ward R C C and Wells M R 2001 Effect of exchange springs on the coercivity of $DyFe_2$–YFe_2 superlattices *J. Magn. Magn. Mater.* **226–230** 1714–16

[15] Bentall M J, Ward R C C and Wells M R 2003 Structure of Laves phase superlattices *J. Phys.: Condens. Matter* submitted

[16] Bowden G J, Bunbury D St P, Guimarães A P and Snyder R E 1968 Mössbauer studies of the cubic Laves iron–rare-earth intermetallic compounds *J. Phys. C: Solid State Phys.* **1** 1376–87

[17] Oderno V, Dufour C, Dumesnil K, Bauer Ph, Mangin Ph, Marchal G, Hennet L and Patrat G 1996 Epitaxially induced anisotropy in thin films of Laves phase compounds *Europhys. Lett.* **36** 713–18

[18] Bland J, Thomas M, Wells M R and Ward R C C 2002 A Mössbauer study of $DyFe_2$, YFe_2, and $HoFe_2$ thin films and multilayers *Phys. Status Solidi* **189** 919–21

[19] Mougin A, Dufour C, Dumesnil K and Mangin Ph 2000 Strain-induced magnetic anisotropy in single crystal RFe_2(110) thin films *Phys. Rev.* B **62** 9517–31

[20] Beaujour J-M L, Bowden G J, Zhukov A A, Rainford B D, de Groot P A J, Ward R C C, Wells M R and Jansen A G M 2003 Anisotropic magneto-resistance in an epitaxial (110) $DyFe_2$ film: a meta-stable magnetic state at 100 K *J. Magn. Magn. Mater.* **257** 270–3

[21] Duc N H 1997 Intersublattice exchange coupling in the lanthanide–transition metal intermetallics *Handbook on the Physics and Chemistry of Rare Earths* vol 24, 1st edn, ed K A Gschneidner Jr and L Eyring (Amsterdam: Elsevier) ch 163, pp 339–98

[22] Oderno V, Dufour C, Dumesnil K, Mangin Ph and Marchal G 1996 Epitaxial growth of (110) $DyFe_2$, $TbFe_2$ thin films by molecular beam epitaxy *J. Cryst. Growth* **165** 175–8

[23] Fullerton E E, Pearson J, Sowers C H, Bader S D, Wu X Z and Sinha S K May 1993 Interfacial roughness of sputtered multilayers: Nb/Si *Phys. Rev.* B **48** 17432–44

[24] Babkevich A Yu, Cowley R A, Mason N J and Stunault A 2000 X-ray scattering, dislocations and orthorhombic GaSb *J. Phys.: Condens. Matter* **12** 4747–56

[25] Smueli U (ed) 1995 *The International Tables for Crystallography* vol C (Amsterdam: Kluwer–Academic)

[26] Bowden G J, Beaujour J M L, Gordeev S, de Groot P A J, Rainford B D and Sawicki M 2000 Discrete exchange-springs in magnetic multilayer samples *J. Phys.: Condens. Matter* **12** 9335–46

[27] Cowley R A and Bates S 1988 The magnetic structure of holmium: I *J. Phys. C: Solid State Phys.* **21** 4113–24

[28] Sawicki M, Bowden G J, de Groot P A J, Rainford B D, Ward R C C and Wells M R 2000 Magnetic properties of epitaxial (110) multilayer films of $DyFe_2$ and YFe_2 *J. Appl. Phys.* **87** 6839–41

[29] Ritter C 1989 Polarised neutron study of the magnetic ordering in the simple alloy YFe_2 *J. Phys.: Condens. Matter* **1** 2765–9